Proximity Induced Superconductivity in Monolayer MoS_2

Daniel J. Trainer[1], BaoKai Wang[2], Fabrizio Bobba[1,3], Noah Samuelson[4], Xiaoxing Xi[1], John Zasadzinski[4], Jouko Nieminen[2,5], Arun Bansil[2], Maria Iavarone[1]*

[1] Physics Department, Temple University, Philadelphia PA 19122, USA

[2] Physics Department, Northeastern University, Boston MA 02115, USA

[3] Physics Department, University of Salerno, Fisciano, 84084, Italy

[4] Physics Department, Illinois Institute of Technology, Chicago IL 60616, USA

[5] Computational Physics Laboratory, Tampere University, Tampere 33014, Finland

ABSTRACT

Proximity effects in superconducting-normal material (SN) heterostructures with metals and semiconductors have long been observed and theoretically described in terms of Cooper pair wavefunctions and Andreev reflections. While the semiconducting N-layer materials in the proximity experiments to date have been doped and tens of nanometers thick, we present here a proximity tunneling study involving a pristine single-layer transition-metal dichalcogenide film of MoS_2 placed on top of a Pb thin-film. Scanning-tunneling microscopy and spectroscopy experiments together with parallel theoretical analysis based on electronic structure calculations and Green's function modeling allow us to unveil a two-step process to be at play in which MoS_2 first becomes metallic and then it is induced into becoming a conventional s-wave Bardeen-Cooper-Schrieffer type superconductor. The lattice mismatch between the MoS_2 overlayer and the Pb substrate is found to give rise to a topographic moiré pattern. Even though the induced gap appears uniform in location, the coherence-peak height of the tunneling spectra is modulated spatially into a moiré pattern that is similar to but shifted with respect to the moiré pattern observed in topography. The aforementioned modulation is shown to originate from the atomic-scale structure of the SN-interface and the nature of local atomic orbitals that are involved in generating the local pairing potential. Our study indicates that the local modulation of induced superconductivity in MoS_2 could be controlled *via* geometrical tuning, and it thus shows promise toward the integration of monolayer superconductors into next-generation functional electronic devices by exploiting proximity-effect control of quantum phases.

KEYWORDS: molybdenum disulfide, monolayer, superconductivity, proximity effect, STM

The possibility of tuning and controlling superconductivity or other symmetry-breaking phenomena in functional materials is at the heart of many possible technological applications. Different pathways can be used to achieve the control of electronic properties. Reducing the dimensionality to engineer heterostructures of different materials has proven to be a successful strategy that has already led to many discoveries in condensed matter physics as well as electronics applications. Low dimensionality leads ultimately to electron confinement that drives changes in material properties and provides opportunities to tune and optimize symmetry-broken-states. Furthermore, heterostructures of different materials offer the capability to selectively tune the coupling between different degree of freedom, where the resulting competition at the interface can drive the appearance of other ground states, *e.g.*, superconductivity between insulators, or ferromagnetism between non-magnetic materials. A milestone in this direction has been the demonstration that charge doping in a field-effect transistor can induce two-dimensional (2D) superconductivity in an insulator (ZrNC).[1] This work inspired the scientific community to induce, by gating, a 2D metallic or superconducting state in monolayer materials. Another milestone has been achieved with misaligned stacks of graphene layers that can be tuned to exhibit extreme electrical behaviors of being an insulator[2] or a superconductor.[3]

Molybdenum disulfide (MoS_2) is a semiconductor with a layered crystal structure consisting of stacked trigonal prismatic monolayers either in a hexagonal (2H) or a rhombohedral (3R) polymorph, whose properties are highly tunable in the monolayer form.[4–10] In the bulk form, chemical intercalation of alkali metals between the adjacent van der Waals MoS_2 layers can be easily achieved and superconductivity can be induced by charge carrier doping[11–13] or by high pressure.[14] Furthermore, field-induced superconductivity at the surface of semiconducting MoS_2 and WS_2 was recently demonstrated[15,16] at low carrier densities. Once doped, the band structure of

these systems presents a rich phenomenology with multiple inequivalent electron pockets at various points of the Brillouin zone (BZ) and gives rise to spin-locking due to the inequivalence of K and K' momentum points in the BZ, and makes the resulting superconductor extremely robust to parallel magnetic fields.[17,18] This unusual superconductor presents a non-BCS like gap[19] and it has been suggested to host topologically non-trivial superconducting states.[20]

Here we report the observation of proximity-induced superconductivity in monolayer MoS_2 adjacent to a Pb film as a conventional s-wave Bardeen-Cooper-Schrieffer (BCS) superconductor. The local superconducting density of states was probed by low-temperature scanning-tunneling microscopy and spectroscopy. Superconductivity can be produced locally when two materials are placed in direct contact.[21] Such proximity-induced superconductivity has been established in metals[22,23] and semiconductors[24,25] placed in contact with low-Tc superconductors. More recently, there has been a renewed interest in semiconductor-superconductor interfaces in search of non-Abelian Majorana fermions in solid-state systems.[26]

Interplay of spin-orbit coupling effects in a MoS_2 monolayer and the superconducting pairing of the substrate can give rise, *via* the proximity effect, to unusual superconducting pairing in MoS_2.[27] However, we find that the gapped density-of-states in the MoS_2 monolayer matches the superconductivity in the underlying layer of Pb (s-wave), and the absence of unconventional superconductivity is similar to what has been reported in the case of proximity-induced superconductivity in graphene grown on Rhenium.[28] In the latter case it has been argued that conventional superconductivity can arise when there is significant charge transfer.[29]

MoS_2 is often treated theoretically as a freestanding two-dimensional sheet and it has been used experimentally as a tunnel barrier.[30,31] Although this appears to be a reasonable model for describing the interface properties in Van der Waals heterostructures, in some experimental

situations there is deviation from this behavior because of physical contact with the environment.[32,33] The Fermi energy of chemical vapor deposition (CVD) grown MoS_2 films lies in the gap but very close to the conduction band edge. Therefore, even weak interactions can shift the Fermi energy into the conduction band.

We have performed theoretical modeling to assess whether or not the superconducting gap and coherence peaks observed in our STS spectra from Pb/MoS_2 heterostructure are due to the proximity effect. The necessary condition for the proximity effect to take place is the presence of interaction-induced MoS_2 delocalized in-gap states. Previous theoretical studies of metallicity in monolayer MoS_2 have been motivated by the need to improve electrical contact between the metal electrodes and MoS_2 layers.[34] In Ref. [34], *ab-initio* calculations were reported for several metals whose orbitals might favorably mix with the Mo-*4d* orbitals. We have analyzed the nature of in-gap states using *ab-initio* and tight-binding calculations and we have determined that these states are hybridized to confirm the metallicity of MoS_2. Furthermore, we have modeled superconductivity by deploying a Hamiltonian with a BCS-type mean field pairing potential for Pb atoms only to confirm that superconductivity can indeed be induced *via* the proximity effect in the MoS_2 monolayer.

The demonstration of transparent interfaces between a BCS superconductor and a MoS_2 monolayer constitutes an important step for developing electronics applications where a metallic contact will be key to improve energy efficiency of the devices.

RESULTS AND DISCUSSION

Moiré superstructure. Scanning tunneling microscopy and spectroscopy (STM/STS) allows us to measure the intrinsic one-electron quasiparticle gap and to correlate it with the local environment at the atomic scale. The heterostructure consisting of a monolayer MoS_2 and a 100 nm thick Pb film was fabricated *ex-situ* as described in the Supporting Information Section I following the "flip-chip" technique[35]; it was back-cleaved in ultra-high vacuum and quickly transferred to the STM scanner at low temperature. This allowed us to perform STM measurements on a fresh surface of MoS_2 and, more importantly, prevent oxidation at the MoS_2/Pb interface. Details of the characterization of a reference Pb film and the Raman measurements confirming the 2H phase of Pb/MoS_2 twin samples can be found in Supporting Information Sections II and III. Figure 1a shows a schematic of the sample measured. In STM images the top S layer of the MoS_2 appears with a typical lattice parameter of 3.2 Å along with the hexagonal moiré superstructure of about 3.3 nm periodicity (Figure 1b), which results from the lattice mismatch between the MoS_2 layer and the Pb substrate. Black regions in this image are likely associated with subsurface defects of the Pb layer since a continuous MoS_2 lattice can be observed, similar to what has been reported for a MoS_2/gold heterostructure.[36] In Figure 1c, a semi-transparent STM topography image is overlaid on the atomic lattice positions of S, Mo and Pb. Here, the S atoms of the simulated MoS_2 lattice are aligned with the S atoms of the measured STM topography. The local environment for each S atom depends on its position. The white trapezoid outlines the unit cell of the moiré pattern where the S atoms overlap the underlying Pb atoms, while the purple trapezoid outlines the lattice positions where the Mo atoms overlap the Pb atoms. Periodicity of the moiré structure is only consistent with Pb(111) lattice parameter of 3.5 Å. An angle of 1.5 degrees is calculated to be the twist-angle between the two layers that produce the observed moiré pattern. A modified Lawer-

Fujita algorithm (Supporting Information Section IV)[37,38] has been used to deduce the lattice distortion and the result shows that the MoS_2 lattice parameter is 3.22 Å and the strain in the MoS_2 monolayer is negligibly small on the order of 0.6%. Furthermore, from a strictly geometrical perspective, the moiré pattern periodicity evolves with twist angle as a monotonic decrease represented by the black curves in Figure 1d[39]:

$$L(\varphi) = \frac{a_{Pb}}{\sqrt{1 + \left(\frac{a_{Pb}}{a_{MoS2}}\right)^2 - 2\left(\frac{a_{Pb}}{a_{MoS2}}\right)cos\varphi}}$$

where L is the moiré lattice periodicity, a_{Pb} and a_{MoS2} are the lattice parameter of the Pb(111) and the MoS_2, respectively, and φ is the twist angle. Similarly, the angle between the moiré pattern and the lattice of the MoS_2 is described by the monotonically increasing function:

$$\vartheta(\varphi) = arcos\left[\frac{\frac{a_{Pb}}{a_{MoS2}}cos\varphi - 1}{\sqrt{1 + \left(\frac{a_{Pb}}{a_{MoS2}}\right)^2 - 2\left(\frac{a_{Pb}}{a_{MoS2}}\right)cos\varphi}}\right]$$

where ϑ is the angle between the moiré pattern and the S-S direction of the MoS_2 lattice. This relationship is represented by the blue curve in Figure 1c. The black and blue curves in Figure 1d show a range of L and ϑ values for an unstrained Pb(111) lattice and one with a 2% strain, indicated by the arrow. From geometrical considerations of the moiré structure, we thus adduce that the two lattices have negligible strain (less than 1% for MoS_2 and less than 2% for Pb). Topography images were found to be independent of energy (Supporting Information Section V).

Metallicity and Superconductivity of MoS_2. In Figure 2 we present the tunneling spectra at high energy on the MoS_2 layer that demonstrate the metallicity of the MoS_2 layer when it is in contact with the Pb(111) substrate. The black curve shows a typical semiconducting spectrum with a gap of 2 eV recorded with the same initial conditions on MoS_2 monolayer prepared in the same

way but not in contact with Pb. The Fermi level lies in the semiconducting gap but quite close to the conduction band edge, typical of films fabricated by CVD.[4] The red curve shows a metallic parabolic spectrum when MoS_2 is placed in contact with Pb(111), indicating an overall strong coupling between the MoS_2 film and the Pb substrate. The tunneling spectrum acquired in the low energy range reveals a superconducting spectrum with a very uniform superconducting gap parameter E_G (Figure 2b). Conductance in the entire gap region is seen to be very similar to that of the reference Pb film, differing only at the coherence peak, where the intensity is always higher than that of the Pb film (Supporting Information Section II). Metallic behavior of the high-bias spectrum indicates that Pb superconductivity is being observed through the proximity effect in the MoS_2 film. Two models of the proximity effect, McMillan[40] and Arnold[41,42], are considered in order to span the range from weak to strong N-S coupling. In the McMillan description of the proximity effect[40] a diffusive barrier is assumed to exist between the normal (N) and superconducting (S) layers. The pair potential $\Delta(r)$ is expected to jump at the NS interface with the jump being reduced upon increasing the transparency of the barrier. Two features are typically observed in this model including a gap-like feature due to the induced pair potential $\Delta_N < \Delta_S$. Here, we observe only a single gap-like feature near the expected value for Pb and so we focus on the Arnold model as outlined below, see Supporting Information Section VI for details.

The conductance map acquired at the energy corresponding to the coherence peak in Figure 2b is shown in Figure 3 together with the topography acquired simultaneously (Figure 3a). The conductance map shows a moiré modulated pattern with the same periodicity as that observed in topography but shifted so that the maximum signal is obtained neither at a S location that overlaps the Pb atoms of the substrate (maximum of the moiré pattern in topography) nor at a location where Mo atoms overlap the Pb atoms, but somewhere in-between these two locations as indicated by

the red trapezoid in Figure 3b, which has been obtained by superimposing the experimental conductance map on the atomic layer structure. The contrast in the conductance map can be understood by recording a full spectrum across a period of the moiré pattern. A line spectroscopy profile consisting of 15 spectra acquired along the white line shown in Figure 3a is given in Figure 3c. The sequence of spectra shows that the energy gap is uniform with location (inset of Figure 3c), but that the coherence peak-height is modulated with the periodicity shown in Figure 3a. Furthermore, no other feature of the tunneling spectrum changes as a function of location.

Given that the period-length of each moiré pattern (3.33 nm) is considerably less than the bulk coherence length of Pb (83 nm), it is unlikely that the conductance peak variation is due to local changes in Pb-superconductivity. Furthermore, it can be argued that the peak modulation is not a consequence of any local variation in the tunneling matrix element. As noted above, Figure 2 shows a background-tunneling conductance at high bias suggestive of vacuum tunneling above a metallic surface. Slight changes in tunneling probability would simply rescale the junction current and would thus be easily compensated by adjusting the tip distance so that a fixed current is obtained at a fixed bias voltage.

As shown in Figure 3 the peak variation is accompanied by a nearly identical above-gap conductance. This suggests an identical normal state (or background) conductance, an effect that is verified by direct measurements above the upper critical field H_{c2}. Thus, the peak variation is a property of the normalized conductance or the local superconducting density of states (DOS). As discussed above, this cannot be coming from the Pb film itself and therefore must be related to the Pb/MoS_2 structure and the associated interface. There is considerable literature available on tunneling into the N side of N/S bilayers[41,42] and it is understood that the surface tunneling density of states, $N_T(E)$, is quite sensitive to the N-layer thickness as well as N/S interface properties such

as quasiparticle transparency and scattering. Such interface properties will be local and related to the atomic overlap of MoS_2 on Pb, which displays the moiré pattern. At a qualitative level, it is therefore reasonable that the peak in $N_T(E)$ would display a moiré pattern as well, and that there is no inherent reason that it would have to be commensurate with the moiré pattern generated by the atomic positions.

For a quantitative analysis, we first define the extrema of the conductance peaks in Figure 3 as "high" and "low". As shown in the inset of Figure 4, the high peak displays a normalized conductance that is higher than the thermally smeared BCS conductance. We note that the low peak is slightly above, but very close to the BCS value. While there are numerous processes that can lead to tunneling conductance peaks that are lower than BCS (*e.g.* inhomogeneities, pairbreaking, McMillan-type proximity effects[40]), there is only one phenomenon we are aware of that can produce a conductance peak that is higher. These are the proximity-effect related structures in the Arnold limit, *i.e.* the specular interface[41,42] can exhibit Andreev bound states at energy $E_0 < \Delta_S$ to produce very sharp conductance peaks in $N_T(E)$, so that the generated normalized conductance exceeds that of BCS. As detailed in Supporting Information Section VII, for ultra-thin N layers, the bound state energy is very close to Δ_S.[43]

There are three main parameters in the Arnold $N_T(E)$[43]. The first, d/l, is the ratio of N layer thickness d and the bulk electron mean free path l at low temperature. Given that the MoS_2 layer is a single monolayer in our case, this parameter will be quite small and we fix it at a value of 0.001, which has minimal effect on $N_T(E)$. The remaining parameters are contained in the expression:

$$R_{eff} = \frac{R(1+r)}{(1-r)}$$

Here $R = 2d/hv_F$ where v_F is the Fermi velocity in the MoS_2 film, a quantity that can be compared to the literature for states near the conduction band valley.[44] The difference in R_{eff} values for the high and low peaks in Figure 3 is thus attributed to differences in the reflection coefficient, r, at the NS interface. Assuming $r = 0$ for the low peak, the larger R_{eff} which gives rise to the bound state pulled down from the continuum, and thus the high peak, has the maximum value of $r = 0.5$. The assumption of the Arnold model is that $r^2 \ll 1$, which is generally satisfied in the fitting of all the conductance spectra, although the maximum value of r only modestly satisfies this condition. Nevertheless, the conductance peaks are seen to fit reasonably well. Deviations of the data from the fit at bias values $eV > E_G$ can be attributed to the strong coupling effects from Pb phonons[45] which are at relatively low energies and are not included in the model.

The analysis above thus presents a very plausible explanation of the moiré pattern that originates from the conductance peaks. The hexagonal structures of the underlying Pb (111) surface and the MoS_2 plane are not perfectly matched, which leads to the moiré pattern associated with atomic positions. This pattern means that there are regions with distinct interface properties, originating in the overlap of atomic orbitals. A local property of the interface, namely the electron reflection coefficient, would thus be expected to vary as well and exhibit its own moiré pattern. Within the Arnold theory, such a variation in r leads to the observed variation in the conductance-peak height. The analysis is consistent with the earlier experimental observations, which conclude that the MoS_2 layer appears to be metallic. Metallicity is also confirmed by the detailed DFT-based calculations of the MoS_2 monolayer on Pb as detailed below.

Theoretical Modeling and Analysis: Metallicity of MoS_2. Theoretical calculations were performed to assess the metallicity of the MoS_2 layer and charge transfer using both *ab-initio* and tight-binding methods. Moreover, we analyzed the proximity-induced superconductivity in the

MoS_2 overlayer using a material-specific tight-binding model including superconducting (SC) pairing. The horizontal lattice structure of MoS_2 was left intact in the computations, while the Pb substrate is allowed to relax in the presence of the MoS_2 overlayer. The justification for this approach is that our experiments suggest that the MoS_2 overlayer is practically unstrained. Since variations of local overlap between orbitals of the interfacial Pb and S atoms are present due to moiré periodicity, we also tested the emergence of in-gap states for a few different relaxation conditions of the substrate and the overlayer.

Our *ab-initio* calculations reveal the emergence of dispersive in-gap bands with a significant contribution from MoS_2, which suggests induced metallicity. This is further supported by our partial-DOS (PDOS) results showing that Mo-*4d* orbitals contribute substantially to the in-gap states. Figure 5a shows the PDOS of the orbitals of MoS_2 obtained on a first-principles basis using the VASP[46] code. The black curve for an artificially free-hanging overlayer (MoS_2) exhibits a clear gap between the valence and conductance bands, while the red curve for the interacting system reveals substantial formation of in-gap states at the Fermi-energy. In Figure 5b, the corresponding band structure is shown in order to check whether the in-gap states are localized or itinerant. The projection of Mo-*4d* orbitals (green markers), indicates that the overlayer related in-gap states crossing the Fermi-level are quite dispersive, which is a signature of itinerant states.

Figure 5c discusses charge-transfer effects by considering the differential charge distribution in the interacting system over the energy range of -0.5 to +0.5eV along the lines of *Popov et al*.[34] A visible differential charge accumulation at the lower part of the MoS_2 overlayer is seen to emerge (see Figure 5d) with a moderate tunneling barrier between the substrate and the overlayer (see Figure 5e). Nevertheless, the supporting tight-binding calculations indicate hybridization between the orbitals of the interfacial Pb and the MoS_2 atoms, and the corresponding PDOS spectra of the

orbitals of the overlayer more or less follow the *ab-initio* results. We also performed comparative tight-binding calculations of differential charge transfer between a non-interacting and interacting system. As shown in Figure 5f-g, a clear accumulation of charge especially in the lower part of the overlayer is observed.

The distance between the substrate and the overlayer controls the overlap between the substrate and overlayer orbitals, and strongly determines the degree of hybridization between these orbitals, which is the key factor responsible for the metallicity of the MoS_2 film. Our conclusion is that in-gap states in MoS_2 overlayer induced *via* its interaction with the normal-state Pb substrate are itinerant, which makes MoS_2 metallic, and makes proximity-induced superconductivity possible. We have carried out computations with different relaxation conditions for the substrate and the overlayer and find that the emergence of in-gap states is a robust feature of our results.

Theoretical Modeling and Analysis: Proximity induced Superconductivity. In our simulations of the SC state, we used a supercell 2x2 times the original cell, but with only three Pb layers in order to help visualize the proximity effect more clearly. We solve the Bogoliubov-deGennes (BdG) equations in a tight-binding basis in terms of a Nambu-Gorkov Green's function.[47,48] Its regular matrix elements, $G(E)$, give the quasiparticle spectrum, which can be compared with the experimental dI/dV spectrum; its anomalous part, $F(E)$, stands for the condensation amplitude, and it can be used to study, *e.g.*, the symmetry and the coherence length of superconductivity. Because of the presence of in-gap states within the MoS_2 layer, the system forms a superconducting-normal (SN) interface. We invoke a pairing potential matrix Δ_S as an input parameter with nonzero elements for only the orbitals of the superconducting subsystem. Solving the Nambu-Gorkov Green's function shows that the spectroscopic gap E_G remains essentially unchanged from the Pb substrate up to the top Sulphur layer since orbital hybridization

across the SN interface is rather strong. As discussed in the Supporting Information Section VI, an induced pair-potential Δ_N is expected to emerge on the normal side due to the proximity effect.[40] Within the present model, $\Delta_N = 0$ except at the interface, where $\Delta_N = -H_{NS}F_{SS}^0(E)H_{SN}^\dagger$, $F_{SS}^0(E)$ is the anomalous Green's function for the non-interacting Pb substrate, and H_{NS} denotes the block of normal-state matrix elements of the Hamiltonian across the SN interface. Our theoretical modeling indicates that the value of Δ_N in the MoS_2 layer vanishes above the interfacial Sulphur layer, implying that the resulting potential well ($\Delta_S - \Delta_N$) will support the presence of an Andreev bound state [42,43] and our use of the Arnold model to explain variations in the intensity of the conductance peak. A limitation of the present model, however, is that the pair potentials Δ_S and Δ_N are not calculated self-consistently from the anomalous Green's function F, and hence the model is not expected to fully capture interference effects between the BCS-type states and the possible Andreev bound states. Nevertheless, the present model convincingly shows the onset of proximity-induced superconductivity by accounting for the superconducting gap and the coherence peaks in terms of the atomic orbitals of the overlayer.

In Figure 6, the most important results related to the superconducting state are shown. The main signature of the proximity effect is shown in Figure 6a, where we give the contributions to the LDOS spectrum from different layers of the substrate and various atoms of the MoS_2 film. Contributions from different layers are scaled to the positive energy dip in the spectrum. A striking evidence for the proximity effect is provided by the fact that both the energy gap and the height of the coherence peaks for the interfacial Pb and S are quite similar to the corresponding results for the middle-layer Mo and surface-layer S, with the coherence peaks being at their highest at the interfacial layers for both Pb and S. Although it is not practical to model the moiré patterns within the framework of our present model, the form of the induced order parameter (off-diagonal self-

energy term) $\sum_{12}^{N}(E) = -H_{NS}F_{SS}^{0}(E)H_{SN}^{\dagger}$ reveals that the local pair potential Δ_N at the interface is laterally inhomogenous, since the interfacial matrix elements of the Hamiltonian are dependent on the distance and bond orientation between the interfacial S and Pb atoms. This indicates that the variation in the gap features against the moiré variation are governed by the local interactions across the SN-interface. In the Supporting Information Section VI, we further discuss how the regular and anomalous self-energies differ from each other and how this leads to different dependencies of the condensation amplitude and the regular LDOS on the local geometry of the interface.

The contribution of different orbitals to the proximity effect can be further characterized by considering the anomalous matrix elements $\boldsymbol{\Phi}_{\alpha\beta}$ of the density-matrix between the orbital α of superconducting Pb and the orbital β of an atom in the overlayer. In a more coarse-grained approach, the coherence length ξ would be a measure of the decay of superconducting pairing across the interface between the S and N subsystems. However, in our tight-binding basis, we do not necessarily see a monotonic decay of this correlation in condensation, but this decay will in general be orbital dependent. In Figure 6b, we see that the off-diagonal elements between the p_z orbital of interfacial Pb and both the d_{z2} and $d_{x2\text{-}y2}$ orbitals of Mo are as high as the matrix element between the Pb and the p_z orbital of the interfacial S. This indicates that there is a significant correlation between the *d*-orbitals of Mo and the orbitals of the substrate Pb, and hence these overlayer orbitals have a dominant role in the proximity effect. The superconducting pairing is still significant up to the surface Sulphur atoms, but the corresponding p_z-p_z matrix elements are relatively small compared to those of Molybdenum *d*-orbitals. The importance of the *d*-orbitals of Mo is also seen in the real-space cross-sectional projections of the anomalous density matrix $\boldsymbol{\Phi}$. Figure 6c shows the horizontal ball-and-stick geometry of the system, and Figure 6d shows the

corresponding cross section of the condensation amplitude $\boldsymbol{\Phi}(\boldsymbol{r}, E)$ at the positive coherence peak 0.2Å above the surface layer of S. The condensation amplitude does not change sign anywhere, which supports the conclusion that superconductivity possesses s-wave symmetry. The vertical cross-sectional visualization of $\boldsymbol{\Phi}(\boldsymbol{r}, E)$ in Figures 6e-g shows the layer-wise evolution of induced superconductivity within the heterostucture. Figure 6e indicates the enhanced nature of the condensation amplitude at the interfacial layers of Pb and S, as the cross-sectional plane is chosen to be at almost equal distance from Pb, S and Mo atoms. On the other hand, as the cross-sectional plane includes the Mo atoms of the overlayer, the strong contribution of the *d*-orbitals at Mo layer is observed in a consistent manner to the off-diagonal matrix elements of the anomalous density matrix in Figure 6b. In addition to giving strong evidence of proximity-induced superconductivity, these results also show the strong local heterogeneity of the condensation amplitude at the atomic scale.

CONCLUSIONS

In this high-resolution STM/STS study, we have investigated Pb(111)/MoS_2 heterostructure and demonstrated proximity-induced superconductivity in the MoS_2 monolayer. *Ab-initio* and material-specific tight-binding calculations show the presence of substantial coupling between the MoS_2 overlayer and the Pb substrate, which induces itinerant in-gap states in MoS_2 and makes it metallic. The induced superconductivity in the MoS_2 overlayer is very similar to the s-wave BCS superconductivity of Pb, with a tunneling spectrum that shows higher coherence peaks compared to the expected BCS value. We find that the modulation of the coherence peak-height of the tunneling spectrum forms a moiré pattern that does not coincide with the moiré pattern observed in topography. We show how this intriguing result could be explained in terms of the local transparency of the interface, which is controlled by orbital overlaps that vary across the interface

and affect the Andreev bound state energy and the tunneling spectrum. These experimental findings coupled with our parallel theoretical modeling show that the coupling between the MoS_2 and Pb layers can potentially be tuned in a controllable way and that the details of interactions between the MoS_2 and Pb orbitals at an atomic-level scale control the proximity effect.

METHODS

Film Growth. Single-layer MoS_2 films were grown on single-side polished, sapphire substrates (University Wafer - C-M plane 0.2^o) using the ambient pressure chemical vapor deposition technique described previously.[4] Prior to the deposition, the substrates were cleaned for 5 minutes in both isopropyl alcohol and acetone using an ultrasonic bath. After the CVD deposition the samples were transferred to a thermal evaporator chamber where Pb pellets (Kurt Lesker – 99.999%) were used to evaporate a 100nm film on top of the MoS_2 in high vacuum (10^{-7}mbar) at an average rate of 1.5 Å/s. Following the "flip-chip" technique described in Ref. [35], a conducting epoxy (Ted Pella H20E) was then applied to the top of the Pb film which was adhered to a Cu sample holding plate used for STM experiments. Similarly, a post was glued to the back side of the sapphire substrate and this structure was placed in the UHV chamber attached to the STM chamber. The sample was cleaved in UHV along the plane in between the sapphire and the MoS_2 film, thus revealing the monolayer MoS_2 film on top of the Pb film. The details of the cleavage are illustrated in Supporting Information Section I.

STM/STS. Scanning-tunneling microscopy and spectroscopy measurements were carried out using a Unisoku STM with PtIr tip in an ultra-high vacuum ($< 10^{-11}$ Torr) at T = 1.5 K. The exposed, post-cleavage, MoS_2 surface was never exposed to air and therefore did not need additional cleaning treatment prior to STM measurement. After cleaving, the sample was

immediately transferred to the cold STM scanner in the adjacent UHV chamber without breaking the vacuum. The PtIr tip used in this experiment was previously prepared on Au single crystal and checked on the surface of a $NbSe_2$ single crystal, cleaved *in-situ*. The STM images were recorded in constant-current mode with tunneling current of 100pA. The dI/dV spectra were recorded using a lock-in technique with a modulation voltage of 10 or 20 mV for the high-energy spectra and 0.2 mV for the low-energy spectra. The modulation frequency used for all spectroscopy was 373.1Hz. I-V curves were acquired simultaneously. An average of 10 spectra per location were acquired. Conductance maps were acquired using the same lock-in parameters used for the point spectroscopy. The conductance values at energies of 0 mV (Fermi energy), 1.6 mV (coherence-peak energy) and 10 mV (above the gap) were recorded at 128 x 128 points over the 15.6 x 15.6 nm^2 area. The set-points parameters used were: V_{set}=10 mV, I=100 pA. Note that conductance maps at low energy show no contrast except for the map acquired at the coherence peak energy. We have used the average value of the conductance map at 10 mV to rescale the conductance map at the coherence peak. This procedure assures that the contrast of the image in not influenced by the single-value rescaling and that the level of noise is the same as the raw data.

AFM. Atomic-force microscopy images were acquired in tapping mode using a Veeco Dimension Icon SPM with an Antimony (n) doped Si tip having a nominal tip radius of 10 nm (Veeco, NCHV). In this mode, the cantilever is driven to oscillate at its resonance frequency of 320 Hz by applying an AC voltage to the z-piezo. A feedback loop is used to fix the tip-sample separation point-by-point in order to keep the amplitude constant. The adjustments in tip-sample distance, driven by the feedback loop, are thus a measure of sample topography. AFM measurements were carried out under ambient conditions.

***Ab-initio* Calculations**. First-principles calculations were performed in the framework of density functional theory (DFT) by using the VASP package.[46] The exchange-correlation functional within the generalized-gradient approximation parameterized by Perdew, Burke and Ernzerhof[49] was used. The slab used to describe the system contained 6-layers of Pb atoms in (111) orientation to model the substrate, one monolayer MoS_2, and a 20Å thick vacuum layer on the top of the heterostructure. The vacuum layer was added to eliminate the interaction with its images. A supercell was constructed by aligning the zigzag direction of MoS_2 and Pb(111) surface. A 2x2 supercell of MoS_2 was set to match $\sqrt{3}$x $\sqrt{3}$ supercell in the substrate. A force criterion of 0.01eV/Å was used in the relaxation procedure of the substrate and the heterostructure. The Brillouin zone of the periodic array of MoS_2/Pb slab was sampled by a 11x11x1 *k*-point grid in the relaxation process, while a denser 19 x 19 x 1 *k*-point grid was used to calculate the density of states.

Tight Binding Calculations: Following references[50,51], we express our model Hamiltonian as follows.

$$H = \sum_{\alpha\beta\sigma}\left(\varepsilon_\alpha c^\dagger_{\alpha\sigma}c_{\alpha\sigma} + V_{\alpha\beta}c^\dagger_{\alpha\sigma}c_{\beta\sigma}\right) + H_{SC} \qquad \text{(T1)}$$

Here $c^\dagger_{\alpha\sigma}(c_{\alpha\sigma})$ is the real-space creation (annihilation) operator, α is a composite index that encodes both the site and orbital information, and σ is the spin index. The on-site orbital energy (ε_α) and the hopping integral between orbitals α and β ($V_{\alpha\beta}$) are obtained within the Slater-Koster formalism[52,53]. Superconductivity is modeled using a BCS-type Hamiltonian in a parametrized form by applying an s-wave-symmetric singlet order parameter $\Delta_{\alpha\sigma\beta-\sigma}$. Accordingly, we write the SC part of the Hamiltonian as:

$$H_{SC} = \sum_{\alpha\beta\sigma}\left(\Delta_{\alpha\sigma\beta-\sigma}c^\dagger_{\alpha\sigma}c^\dagger_{\beta-\sigma} + h.c.\right). \qquad \text{(T2)}$$

The order parameter $\Delta_{\alpha\sigma\beta-\sigma}$ is non-zero only for the onsite matrix elements ($\beta = \alpha$) of the *s*- and *p*-orbitals of Pb atoms. We have artificially enhanced the amplitudes of the matrix elements, since modeling a narrow energy range would also require a dense *k*-point mesh. Nevertheless, the trends in gap-width and coherence peak-heights are not sensitive to the absolute value of the order parameter.

This Hamiltonian effectively leads to Bogoliubov- deGennes equations, which can be used to derive the Nambu-Gorkov tensor Green's function[47,48]

$$\boldsymbol{G} = \begin{pmatrix} G_e & F \\ F^{\dagger} & G_h \end{pmatrix} \qquad \text{(T3)}$$

which consists of the regular Green's functions G_e and G_h for electrons and holes along the diagonal, and the anomalous Green's functions $F^{\dagger}$ and $F^{\dagger}$as off-diagonal blocks. The regular quasiparticle spectrum is derived from the regular part of the Green's function

$$\boldsymbol{\rho}_{\alpha\beta} = -\frac{1}{2\pi i}(G - G^{\dagger})_{\alpha\beta} \qquad \text{(T4)}$$

The electron-hole pairing amplitudes between orbitals α and β can be extracted from the anomalous terms of the density matrix

$$\boldsymbol{\Phi}_{\alpha\beta} = -\frac{1}{2\pi i}(F - F^{\dagger})_{\alpha\beta} \qquad \text{(T5)}$$

Furthermore, matrix $\boldsymbol{\Phi}$ can be transformed into real space cross-sections to visualize the symmetry of pairing as is done in Figure 6 by using Slater orbitals as a real-space presentation of the basis.

ASSOCIATED CONTENT

Supporting Information

Supporting Information on sample fabrication, characterization and modified real-space Lawler-Fujita Algorithm as well as the relationship between the present theoretical model and the McMillan and Arnold formalisms is available free of charge *via* the Internet at http://pubs.acs.org.

The authors declare no competing financial interests.

AUTHOR INFORMATION

Corresponding Author

*E-mail iavarone@temple.edu

Author Contributions. D. J. Trainer, F. Bobba performed low temperature STM/STS measurements under guidance of M. Iavarone at Temple University. D. J. Trainer fabricated MoS_2 films under guidance of X. X. Xi and he characterized the samples with AFM/STM and transport at Temple University under guidance of M. Iavarone. J. Zasadzinski and N. Samuelson performed the analysis of the tunneling spectra based on the proximity model and the Raman characterization of the samples. B. Wang, J. Nieminen and A. Bansil carried out the theoretical computations and analysis. All authors participated in the writing of the manuscript.

ACKNOWLEDGEMENTS

The work at Temple University was supported by the US Department of Energy (DOE), Office of Science, Basic Energy Sciences, Division of Materials Sciences and Engineering, under grant No. DE-SC0004556 (Superconducting heterostructures fabrication, surface preparation, superconducting characterization) and by the Center for Complex Materials from First Principles (CCM), an Energy Frontier Research Center funded by the U.S. Department of Energy,

Office of Science, Basic Energy Sciences under Award No. DE-SC0012575 (Two-dimensional materials growth and characterization). The work at Northeastern University was supported by the US Department of Energy (DOE), Office of Science, Basic Energy Sciences grant number DEFG02-07ER46352 (core research), and benefited from Northeastern University's Advanced Scientific Computation Center (ASCC), the NERSC supercomputing center through DOE grant number DE-AC02-05CH11231, and support from the DOE grant number DE-SC0019275 for work on proximity effects in heterostructures for developing next-generation qubits. This work benefited from the resources of the Institute of Advanced Computing, Tampere.

REFERENCES

(1) Ye, J. T.; Inoue, S.; Kobayashi, K.; Kasahara, Y.; Yuan, H. T.; Shimotani, H.; Iwasa, Y. Liquid-Gated Interface Superconductivity on an Atomically Flat Film. *Nat. Mater.* **2010**, *9*, 125–128.

(2) Cao, Y.; Fatemi, V.; Demir, A.; Fang, S.; Tomarken, S. L.; Luo, J. Y.; Sanchez-Yamagishi, J. D.; Watanabe, K.; Taniguchi, T.; Kaxiras, E.; Ashoori, R.C.; Jarillo-Herrero, P. Correlated Insulator Behaviour at Half-Filling in Magic-Angle Graphene Superlattices. *Nature* **2018**, *556*, 80–84.

(3) Cao, Y.; Fatemi, V.; Fang, S.; Watanabe, K.; Taniguchi, T.; Kaxiras, E.; Jarillo-Herrero, P. Unconventional Superconductivity in Magic-Angle Graphene Superlattices. *Nature* **2018**, *556*, 43–50.

(4) Trainer, D. J.; Putilov, A. V.; Di Giorgio, C.; Saari, T.; Wang, B.; Wolak, M.; Chandrasena, R. U.; Lane, C.; Chang, T.-R.; Jeng, H.-T.; Lin, H.; Kronast, F.; Gray, A.X.; Xi, X.; Nieminen, J.; Bansil, A.; Iavarone, M. Inter-Layer Coupling Induced Valence Band Edge Shift in Mono- to Few-Layer MoS_2. *Sci. Rep.* **2017**, *7*, 40559.

(5) Trainer, D. J.; Putilov, A. V.; Wang, B.; Lane, C.; Saari, T.; Chang, T.-R.; Jeng, H.-T.; Lin, H.; Xi, X.; Nieminen, J.; Bansil, A.; Iavarone, M. Moiré Superlattices and 2D Electronic Properties of Graphite/MoS_2 Heterostructures. *J. Phys. Chem. Solids* **2019**, *128*, 325–330.

(6) Liu, K.; Zhang, L.; Cao, T.; Jin, C.; Qiu, D.; Zhou, Q.; Zettl, A.; Yang, P.; Louie, S. G.; Wang, F. Evolution of Interlayer Coupling in Twisted Molybdenum Disulfide Bilayers. *Nat. Commun.* **2014**, *5*, 4966.

(7) van der Zande, A. M.; Kunstmann, J.; Chernikov, A.; Chenet, D. A.; You, Y.; Zhang, X.; Huang, P. Y.; Berkelbach, T. C.; Wang, L.; Zhang, F.; Hybertsen, M.S.; Muller, D.A.; Reichman, D.R.; Heinz, T.F.; Hone, J.C. Tailoring the Electronic Structure in Bilayer Molybdenum Disulfide *via* Interlayer Twist. *Nano Lett.* **2014**, *14*, 3869.

(8) Huang, Y. L.; Che, Y.; Zhang, W.; Quek, S.Y.; Chen, C.-H.; Li, L.-J.; Hsu, W.-T.; Chang, W.-H.; Zheng, Y. J.; Chen, W.; and Wee, A.T.S. Bandgap Tunability at Single-Layer Molybdenum Disulphide Grain Boundaries. *Nat. Commun.* **2015**, 6, 6298.

(9) Jin, W.; Yeh, P.-C.; Zaki, N.; Chenet, D.; Arefe, G.; Hao, Y.; Sala, A.; Mentes, T. O.; Dadap, J. I.; Locatelli, A.; Hone, J.; Osgood, R.M. Jr. Tuning the Electronic Structure of Monolayer Graphene/MoS_2 van Der Waals Heterostructures *via* Interlayer Twist. *Phys. Rev. B* **2015**, *92*, 201409.

(10) Zhao, M.; Ye, Z.; Suzuki, R.; Ye, Y.; Zhu, H.; Xiao, J.; Wang, Y.; Iwasa, Y.; Zhang, X. Atomically Phase-Matched Second-Harmonic Generation in a 2D Crystal. *Light: Sci. Appl.* **2016**, *5*, e16131.

(11) Somoano, R. B.; Rembaum, A. Superconductivity in Intercalated Molybdenum Disulfide. *Phys. Rev. Lett.* **1971**, *27*, 402–404.

(12) Woollam, J. A.; Somoano, R. B. Superconducting Critical Fields of Alkali and Alkaline-Earth Intercalates of MoS_2. *Phys. Rev. B* **1976**, *13*, 3843–3853.

(13) Zhang, R.; Tsai, I.-L.; Chapman, J.; Khestanova, E.; Waters, J.; Grigorieva, I. V. Superconductivity in Potassium-Doped Metallic Polymorphs of MoS_2. *Nano Lett.* **2016**, *16*, 629–636.

(14) Chi, Z.; Chen, X.; Yen, F.; Peng, F.; Zhou, Y.; Zhu, J.; Zhang, Y.; Liu, X.; Lin, C.; Chu, S.; Li, Y.; Zhao, J.; Kagayama, T. Superconductivity in Pristine $2H_a$–MoS_2 at Ultrahigh Pressure. *Phys. Rev. Lett.* **2018**, *120*, 037002.

(15) Ye, J. T.; Zhang, Y. J.; Akashi, R.; Bahramy, M. S.; Arita, R.; Iwasa, Y. Superconducting Dome in a Gate-Tuned Band Insulator. *Science* **2012**, *338*, 1193–1196.

(16) Jo, S.; Costanzo, D.; Berger, H.; Morpurgo, A. F. Electrostatically Induced Superconductivity at the Surface of WS_2. *Nano Lett.* **2015**, *15*, 1197–1202.

(17) Lu, J. M.; Zheliuk, O.; Leermakers, I.; Yuan, N. F. Q.; Zeitler, U.; Law, K. T.; Ye, J. T. Evidence for Two-Dimensional Ising Superconductivity in Gated MoS_2. *Science* **2015**, *350*, 1353–1357.

(18) Saito, Y.; Nakamura, Y.; Bahramy, M. S.; Kohama, Y.; Ye, J.; Kasahara, Y.; Nakagawa, Y.; Onga, M.; Tokunaga, M.; Nojima, T.; Yanase, Y.; Iwasa, Y. Superconductivity Protected by Spin–Valley Locking in Ion-Gated MoS_2. *Nat. Phys.* **2016**, *12*, 144–149.

(19) Costanzo, D.; Zhang, H.; Reddy, B. A.; Berger, H.; Morpurgo, A. F. Tunnelling Spectroscopy of Gate-Induced Superconductivity in MoS_2. *Nat. Nanotechnol.* **2018**, *13*, 483–488.

(20) Hsu, Y.-T.; Vaezi, A.; Fischer, M. H.; Kim, E.-A. Topological Superconductivity in Monolayer Transition Metal Dichalcogenides. *Nat. Commun.* **2017**, *8*, 14985.

(21) Wolf, E. L. Proximity Effect Tunneling. *Physica B+C* **1982**, *109, 110B*, 1722–1736.

(22) Werthamer, N. R. Theory of the Superconducting Transition Temperature and Energy Gap Function of Superposed Metal Films. *Phys. Rev.* **1963**, *132*, 2440–2445.

(23) Clarke, J. The Proximity Effect Between Superconducting and Normal Thin Films in Zero Field. *Colloq. Phys.* **1968**, *29*, C2-3.

(24) Kastalsky, A.; Kleinsasser, A. W.; Greene, L. H.; Bhat, R.; Milliken, F. P.; Harbison, J. P. Observation of Pair Currents in Superconductor-Semiconductor Contacts. *Phys. Rev. Lett.* **1991**, *67*, 3026–3029.

(25) Nguyen, C.; Kroemer, H.; Hu, E. L. Anomalous Andreev Conductance in InAs-AlSb Quantum Well Structures with Nb Electrodes. *Phys. Rev. Lett.* **1992**, *69*, 2847–2850.

(26) Fu, L.; Kane, C. L.; Mele, E. J. Topological Insulators in Three Dimensions. *Phys. Rev. Lett.* **2007**, *98*, 106803.

(27) Triola, C.; Badiane, D. M.; Balatsky, A. V.; Rossi, E. General Conditions for Proximity-Induced Odd-Frequency Superconductivity in Two-Dimensional Electronic Systems. *Phys. Rev. Lett.* **2016**, *116*, 257001.

(28) Tonnoir, C.; Kimouche, A.; Coraux, J.; Magaud, L.; Delsol, B.; Gilles, B.; Chapelier, C. Induced Superconductivity in Graphene Grown on Rhenium. *Phys. Rev. Lett.* **2013**, *111*, 246805.

(29) Khomyakov, P. A.; Giovannetti, G.; Rusu, P. C.; Brocks, G.; van den Brink, J.; Kelly, P. J. First-Principles Study of the Interaction and Charge Transfer between Graphene and Metals. *Phys. Rev. B* **2009**, *79*, 195425.

(30) Dvir, T.; Massee, F.; Attias, L.; Khodas, M.; Aprili, M.; Quay, C. H. L.; Steinberg, H. Spectroscopy of Bulk and Few-Layer Superconducting NbSe2 with van Der Waals Tunnel Junctions. *Nat. Commun.* **2018**, *9*, 598.

(31) Dvir, T.; Aprili, M.; Quay, C. H. L.; Steinberg, H. Tunneling into the Vortex State of $NbSe_2$ with van Der Waals Junctions. *Nano Lett.* **2018**, *18*, 7845–7850.

(32) Zhong, H.; Quhe, R.; Wang, Y.; Ni, Z.; Ye, M.; Song, Z.; Pan, Y.; Yang, J.; Yang, L.; Lei, M.; Shi, J.; Lu, J. Interfacial Properties of Monolayer and Bilayer MoS_2 Contacts with Metals: Beyond the Energy Band Calculations. *Sci. Rep.* **2016**, *6*, 21786.

(33) Li, F.; Lu, Z.; Lan, Y.-W.; Jiao, L.; Xu, M.; Zhu, X.; Zhang, X.; Wu, H.; Qi, J. Force and Light Tuning Vertical Tunneling Current in the Atomic Layered MoS_2. *Nanotechnology* **2018**, *29*, 275202.

(34) Popov, I.; Seifert, G.; Tománek, D. Designing Electrical Contacts to MoS_2 Monolayers: A Computational Study. *Phys. Rev. Lett.* **2012**, *108*, 156802.

(35) Flötotto, D.; Ota, Y.; Bai, Y.; Zhang, C.; Okazaki, K.; Tsuzuki, A.; Hashimoto, T.; Eckstein, J. N.; Shin, S.; Chiang, T.-C. Superconducting Pairing of Topological Surface States in Bismuth Selenide Films on Niobium. *Sci. Adv.* **2018**, *4*, eaar7214.

(36) Krane, N.; Lotze, C.; Läger, J. M.; Reecht, G.; Franke, K. J. Electronic Structure and Luminescence of Quasi-Freestanding MoS_2 Nanopatches on Au(111). *Nano Lett.* **2016**, *16*, 5163–5168.

(37) Lawler, M. J.; Fujita, K.; Lee, J.; Schmidt, A. R.; Kohsaka, Y.; Kim, C. K.; Eisaki, H.; Uchida, S.; Davis, J. C.; Sethna, J. P.; Kim, E.-A. Intra-Unit-Cell Electronic Nematicity of the High-Tc Copper-Oxide Pseudogap States. *Nature* **2010**, *466*, 347–351.

(38) Trainer, D. J.; Zhang, Y.; Bobba, F.; Xi, X.; Hla, S.-W.; Iavarone, M. The Effects of Atomic-Scale Strain Relaxation on the Electronic Properties of Monolayer MoS_2. *ACS Nano* **2019**, *13*, 8284–8291.

(39) Zeller, P.; Günther, S. What Are the Possible Moiré Patterns of Graphene on Hexagonally Packed Surfaces? Universal Solution for Hexagonal Coincidence Lattices, Derived by a Geometric Construction. *New J. Phys.* **2014**, *16*, 083028.

(40) McMillan, W. L. Tunneling Model of the Superconducting Proximity Effect. *Phys. Rev.* **1968**, *175*, 537–542.

(41) Wolf, E. L. Electron Tunneling Spectroscopy, 2nd Ed. (Oxford University Press, Oxford) 2012.

(42) Wolf, E. L.; Zasadzinski, J.; Osmun, J. W.; Arnold, G. B. Proximity Electron Tunneling Spectroscopy I. Experiments on Nb. *J. Low Temp. Phys.* **1980**, *40*, 19–50.

(43) Wolf, E. L.; Arnold, G. B. Proximity Electron Tunneling Spectroscopy. *Phys. Rep.* **1982**, *91*, 31–102.

(44) Rose, F.; Goerbig, M. O.; Piéchon, F. Spin- and Valley-Dependent Magneto-Optical Properties of MoS_2. *Phys. Rev. B* **2013**, *88*, 125438.

(45) McMillan, W. L.; Rowell, J. M. *Superconductivity*, R.D. Parks, ed.; Dekker, New York, 1969; Vol. I.

(46) Kresse, G.; Hafner, J. *Ab Initio* Molecular Dynamics for Liquid Metals. *Phys. Rev. B* **1993**, *47*, 558–561.

(47) De Gennes, P. G. Boundary Effects in Superconductors. *Rev. Mod. Phys.* **1964**, *36*, 225–237.

(48) Abrikosov, A. A.; Gorkov, L. P.; Dzyaloshinkii, I. *Methods of Quantum Field Theory in Statistical Physics*; New York, NY: Dover, 1975.

(49) Perdew, J. P.; Burke, K.; Ernzerhof, M. Generalized Gradient Approximation Made Simple. *Phys. Rev. Lett.* **1996**, *77*, 3865–3868.

(50) Saari, T.; Nieminen, J.; Bansil, A. Spectroscopic Signatures of Different Symmetries of the Superconducting Order Parameter in Metal-Decorated Graphene. *J. Phys.: Condens. Matter* **2017**, *29*, 215601.

(51) Nieminen, J.; Suominen, I.; Das, T.; Markiewicz, R. S.; Bansil, A. Evidence of Strong Correlations at the van Hove Singularity in the Scanning Tunneling Spectra of Superconducting $Bi_2Sr_2CaCu_2O_{8+\delta}$ Single Crystals. *Phys. Rev. B* **2012**, *85*, 214504.

(52) Slater, J. C.; Koster, G. F. Simplified LCAO Method for the Periodic Potential Problem. *Phys. Rev.* **1954**, *94*, 1498–1524.

(53) Harrison, W. A. Electronic Structure and the Properties of Solids - The Physics of the Chemical Bond; Dover:New York (1989).

Figures

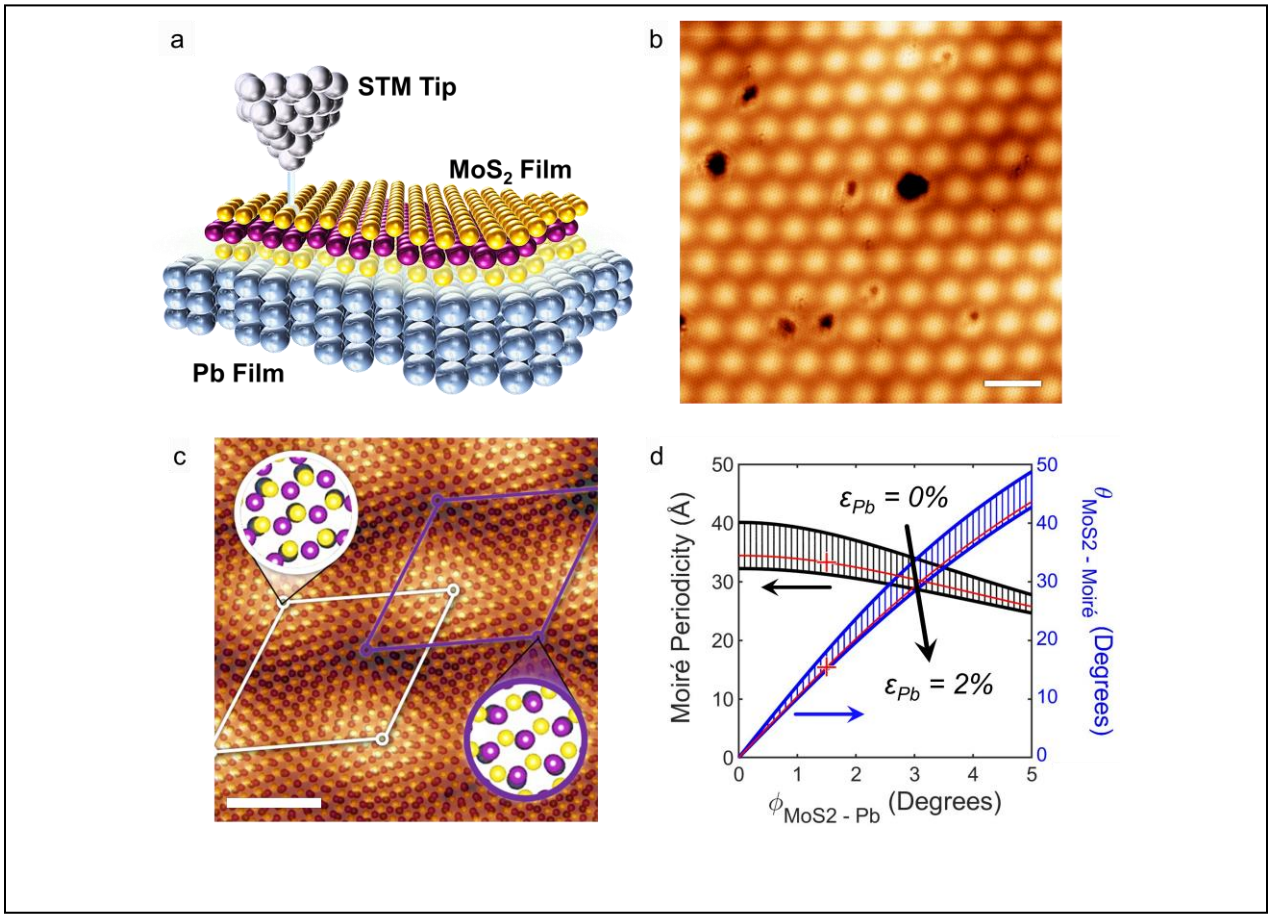

Figure 1. Moiré pattern of MoS_2 on Pb(111) a, A 3D schematic of the STM measurement on one monolayer of MoS_2 on a Pb(111) surface. **b,** STM topography of the monolayer MoS_2 film on Pb (V = 50 mV, I = 100 pA). The scale-bar represents 5nm. **c,** A model depicting the atomic positions of S, Mo and Pb atoms with a semi-transparent STM topography overlaid (V = 10 mV, I = 100 pA). The atoms in the STM topography are aligned with the S atoms in the model. The white (purple) trapezoid outlines the unit cell of the moiré pattern where the S (Mo) atoms overlap the Pb atoms. The scale-bar represents 2nm. **d,** The dependence of the moiré periodicity (black lines) and of the angle between the moiré pattern and MoS_2 (blue lines) as a function of rotation between the MoS_2 and Pb lattices. The black and the blue highlighted regions represent the range of values of L and ϑ from an unstrained Pb film (topmost curves) up to a 2% strain of the Pb film (bottom-most curves). The red crosses represent the measured values where the MoS_2/Pb angle of 1.5° was obtained by the model in Figure 1c.

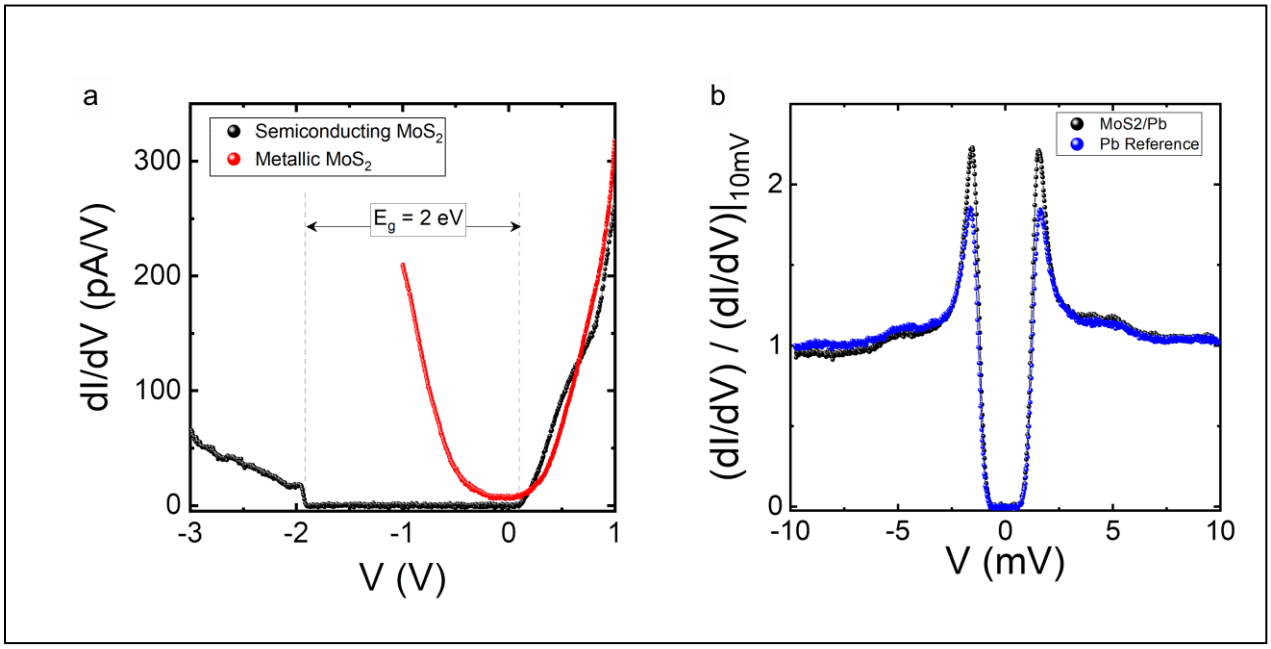

Figure 2. Metallicity and superconductivity of MoS_2 monolayer on Pb(111). A comparison between the metallic spectrum measured on the topography of Fig.1a with a typical spectrum measured on MoS_2 displaying semiconducting behavior acquired with the same stabilization voltage (V_{set} = 1.0 V, I = 100 pA). **b,** A low-energy spectrum acquired on MoS_2/Pb (black) is compared with a typical spectrum acquired on the reference Pb film (blue) (V_{set} = 10 mV, I = 100 pA, Vmod=0.2 mV, T=1.5 K). The spectra have been normalized by their value of conductance at V=10 mV.

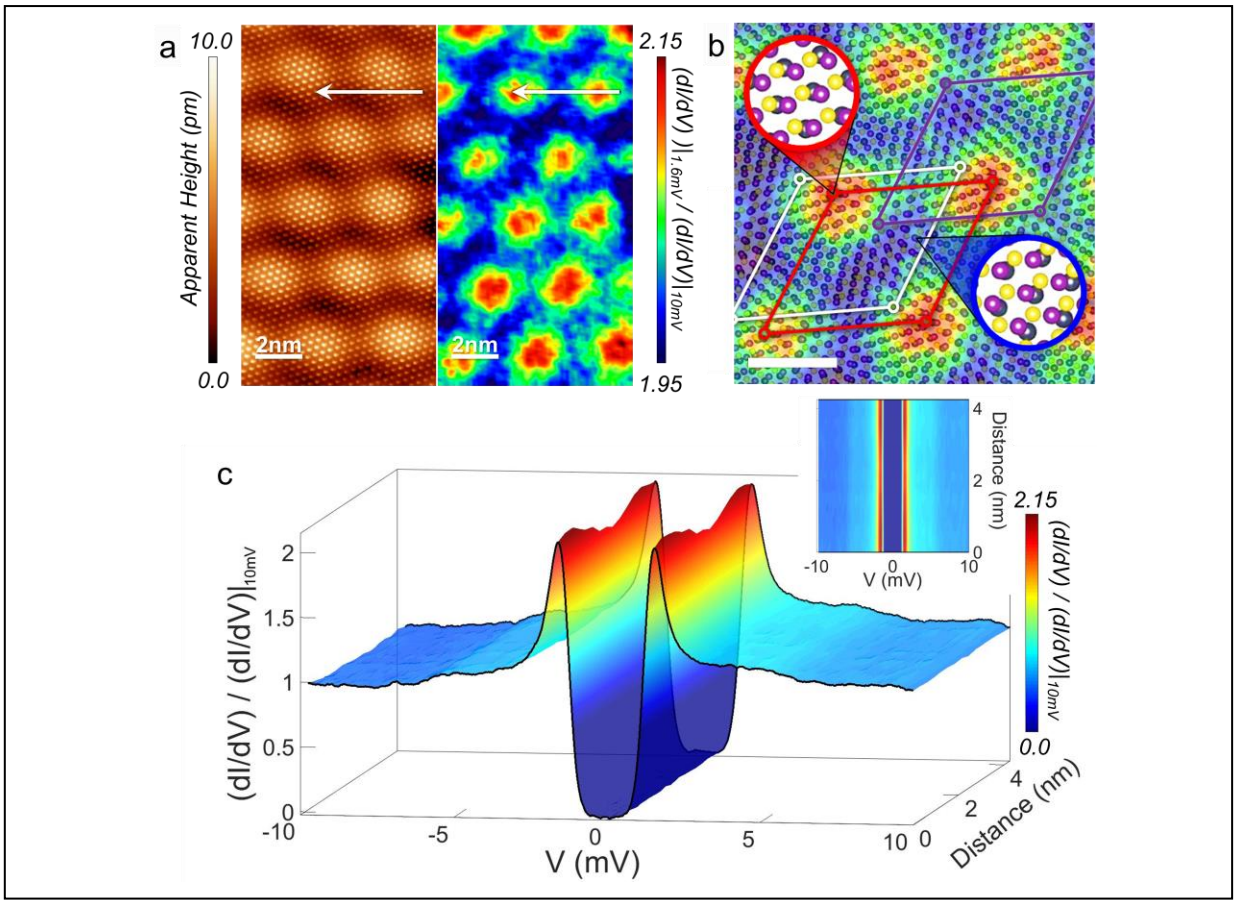

Figure 3. Modulation of superconductivity with the topographical moiré pattern. a, Left panel shows the STM topography and the right panel shows the conductance map recorded at the energy corresponding to the coherence peak in the tunneling spectrum (V=1.6 mV). The conductance map at the coherence peak energy (1.6 mV) was normalized to the average value of the distribution of the normal state conductance map (10 mV). The conductance signal shows modulations that form a moiré pattern with the same periodicity as that measured in topography. **b,** The model from Fig. 1b with a semi-transparent conductance map at the energy of the coherence peak overlaid showing the positions of the maxima in the map relative to the atomic positions. The red trapezoid represents the unit cell of the modulation of the conductance map. **c,** A series of 15 spectra acquired over the white lines in Fig. 3a (V_{set} = 10 mV, I = 100 pA). The tunneling spectra were normalized by their value of conductance at V=10 mV. The inset gives the top view of the tunneling spectra and shows the uniformity of the gap across the moiré period.

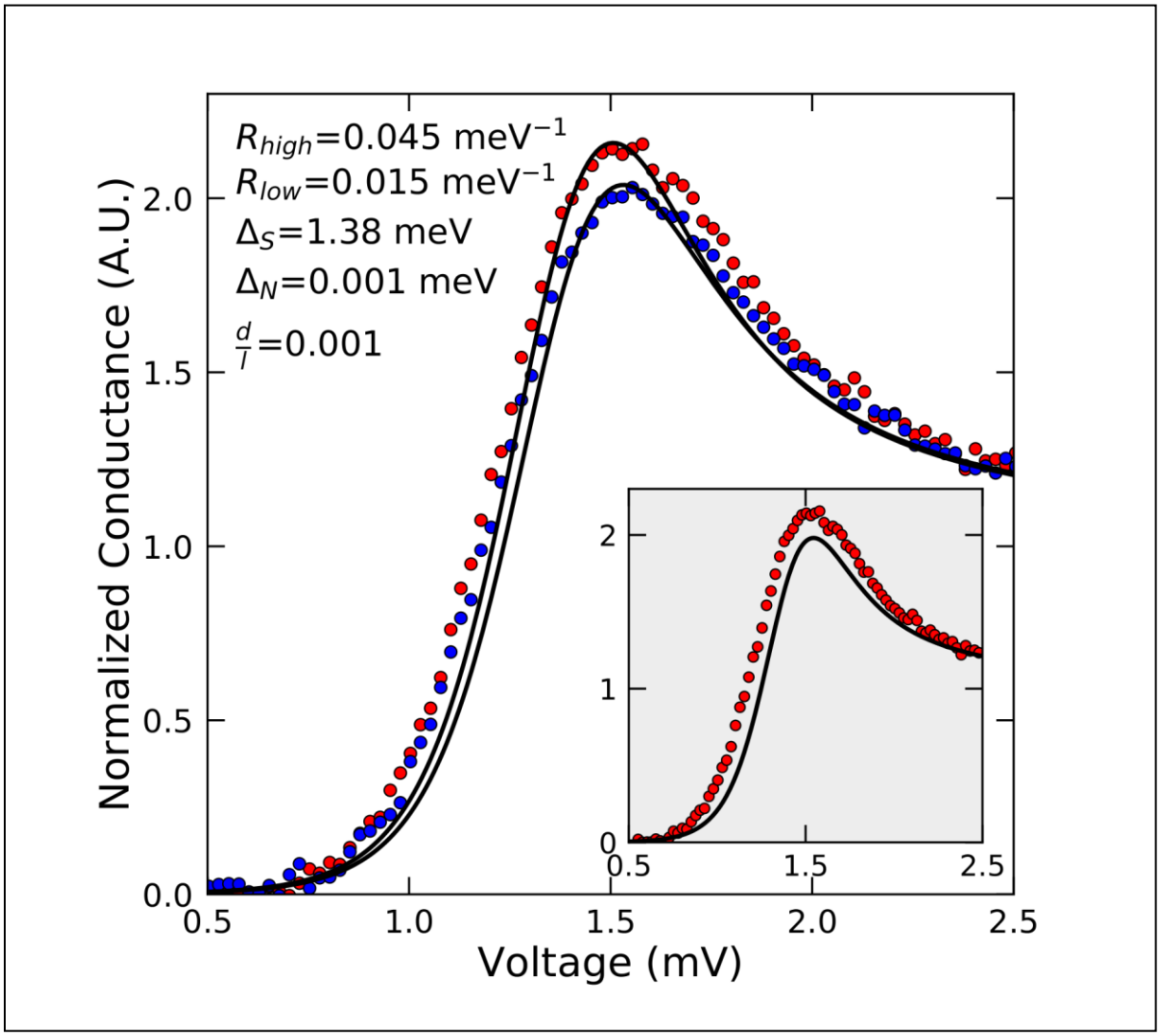

Figure 4. Proximity analysis of the low-energy tunneling spectra. Tunneling conductance data exhibiting the high peak (red dots) and low peak (blue dots) at the extrema of Figure 3c. The tunneling conductance spectra have been normalized to the normal-state conductance spectrum. Theoretical fits using the Arnold theory are shown as solid-black lines with R_{eff} values indicated. Inset shows the high-peak data compared to an ideal BCS conductance for Δ= 1.38 meV at the measured temperature T=1.5K. Inset shows the high-peak data compared to an ideal BCS conductance for Δ= 1.38 meV at the measured temperature T=1.5K.

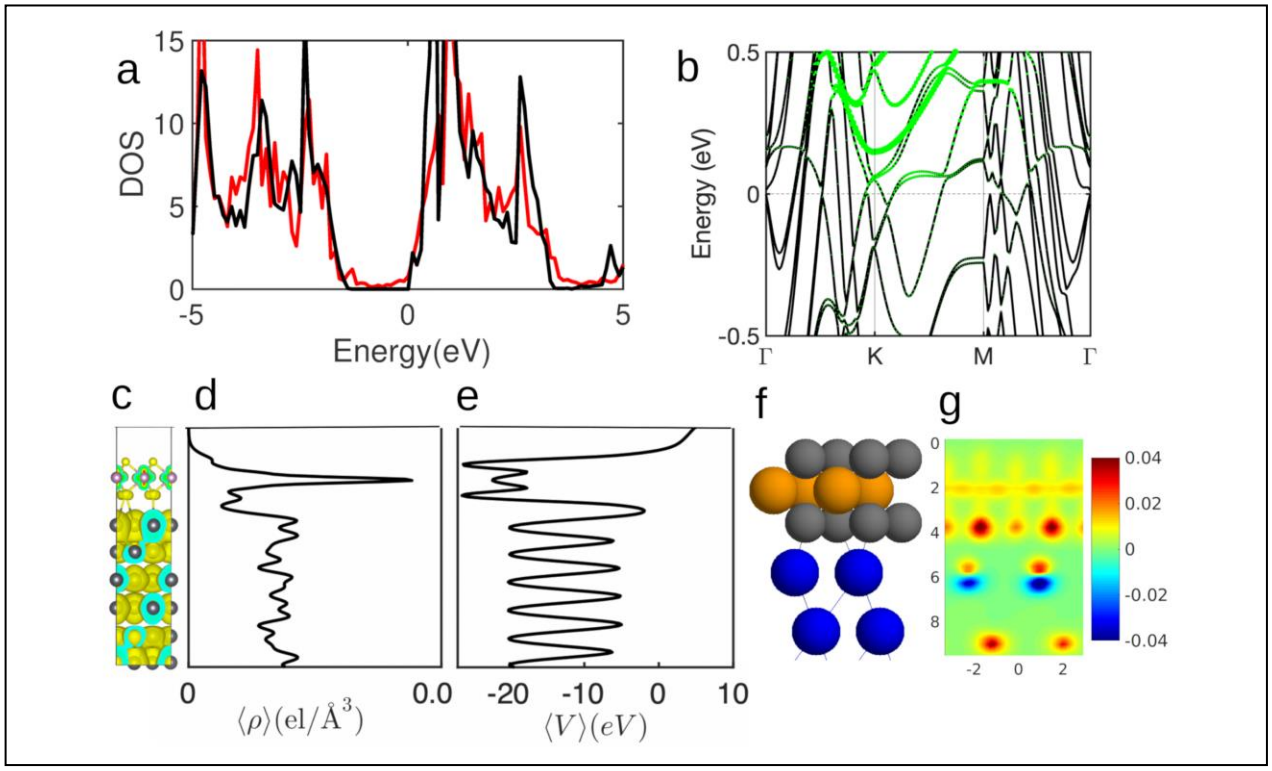

Figure 5. Induced metallicity of the MoS_2 overlayer. **a**, PDOS projected onto the orbitals of MoS_2 for non-interacting (black curve) and interacting (red curve) MoS_2/Pb system; **b**, The band structure of MoS_2 with projection of the d-orbitals of Mo atoms; **c**, The partial charge density (between -0.5 and +0.5eV) of MoS_2 on Pb(111); **d**, the z-dependence of the partial charge density of **c**; and **e**, the corresponding potential energy of electrons; **f**, a ball-and-stick model for tight-binding calculations; **g**, the differential charge compared to a non-interacting system.

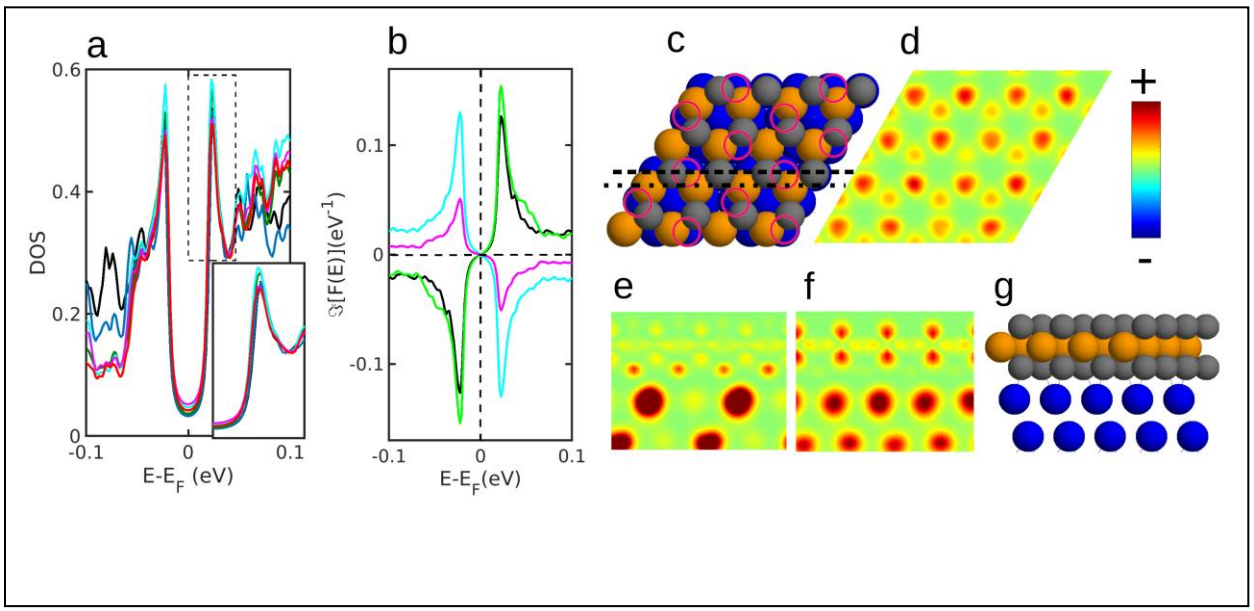

Figure 6. Spatial variation of the density of states and the pairing amplitude. a, Scaled PDOS of (s + 3*p*)-orbitals of the bottom (black, scaling factor *x*1.0), middle (blue, *x*2.03) and interfacial Pb (green, *x*1.14), interfacial S (cyan, *x*14.8), (s+5*d*)-orbitals of Mo (red, *x*9.54) and *p*-orbitals of surface S (magenta, *x*35.6). A magnified plot around the positive energy peak is shown in the insert; **b**, The off-diagonal elements of $\boldsymbol{\Phi}_{\alpha\beta}$ between the p_z-orbital of a top-layer Pb atom, and the selected orbitals of MoS_2 overlayer: p_z of an interfacial S (cyan), d_{x2-y2} of Mo (green), d_{z2} of Mo (black) and p_z of the top layer S (magenta). **c**, Geometric structure of the system in tight-binding calculations. S, Mo, and Pb atoms are denoted by gray, beige and blue spheres, respectively. The red circles indicate the horizontal position of the interface layer Pb atoms. **d**, The horizontal cross section of the pairing amplitude maps $\boldsymbol{\Phi}(\boldsymbol{r}, E)$ at the positive energy coherence peak at 0.2 Å above the surface S layer. **e**, and **f**, The vertical cross-section of the pairing amplitude maps $\boldsymbol{\Phi}(\boldsymbol{r}, E)$ at the positive energy coherence peak. The cross-sectional planes follow the dashed line and the dash-dotted line of (c), respectively. **g**, The side view of the simulation cell corresponding to **e** and **f**.

For Table of Content Only

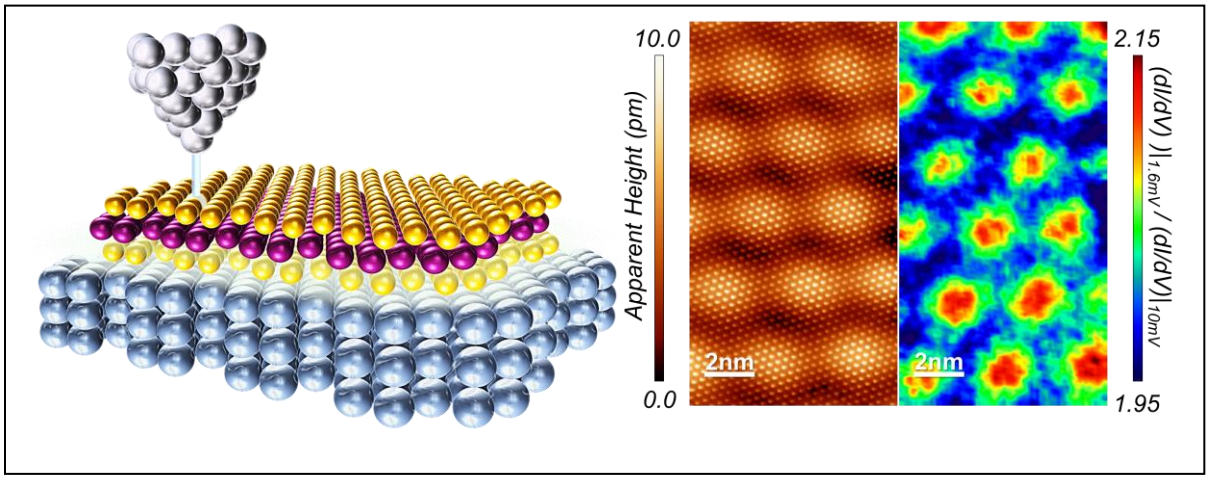

SUPPORTING INFORMATION

Proximity Induced Superconductivity in Monolayer MoS_2

Daniel J. Trainer[1], BaoKai Wang[2], Fabrizio Bobba[1,3], Noah Samuelson[4], Xiaoxing Xi[1], John Zasadzinski[4], Jouko Nieminen[2,5], Arun Bansil[2], Maria Iavarone[1]*

[1] Physics Department, Temple University, Philadelphia PA 19122, USA

[2] Physics Department, Northeastern University, Boston MA 02115, USA

[3] Physics Department, University of Salerno, Fisciano, 84084, Italy

[4] Physics Department, Illinois Institute of Technology, Chicago IL 60616, USA

[5] Computational Physics Laboratory, Tampere University, Tampere 33014, Finland

CONTENT

I. Sample Preparation

The samples were prepared with the intent to preserve the Pb/MoS_2 interface. This was achieved by never exposing to air the Pb surface in contact with the MoS_2. A step-by-step description of this process is given in Fig. S1. First a monolayer film of MoS_2 was grown on a sapphire substrate by the ambient pressure chemical vapor deposition (APCVD) technique. The as-grown film is shown in the AFM topography of Fig. S1a. Next, the sample was loaded into a thermal evaporator where 100 nm of Pb was deposited on top of the film at a rate of approximately 1.5 Å/s measured with a quartz crystal monitor. MoS_2 and Pb films were grown in separate chambers and the MoS_2 was handled with care to reduce water contamination. The structure was then flipped over so that the Pb film adhered to the Cu sample plate, used for STM measurements, using a conductive epoxy. A cleaving post was adhered to the back side of the sapphire substrate using the same epoxy. The structure was then loaded into a UHV chamber. When the chamber reached its base pressure, the post was knocked off. This motion cleaves the structure along the

plane lying between the MoS_2 film and sapphire due to weak van der Waals adhesion. The resulting structure yields the monolayer of MoS_2 on top of the Pb film. The interface between the MoS_2 and Pb film was never exposed to air, so that oxidation of the Pb layer was prevented. After cleavage, the sample was moved to the cold STM scanner without breaking the vacuum. The AFM topography of a twin sample after the cleaving process is shown in Fig. S1b. This twin sample was measured in ambient conditions, causing the exposed Pb to oxidize, explaining why the exposed Pb has a higher topographic height than the MoS_2 islands.

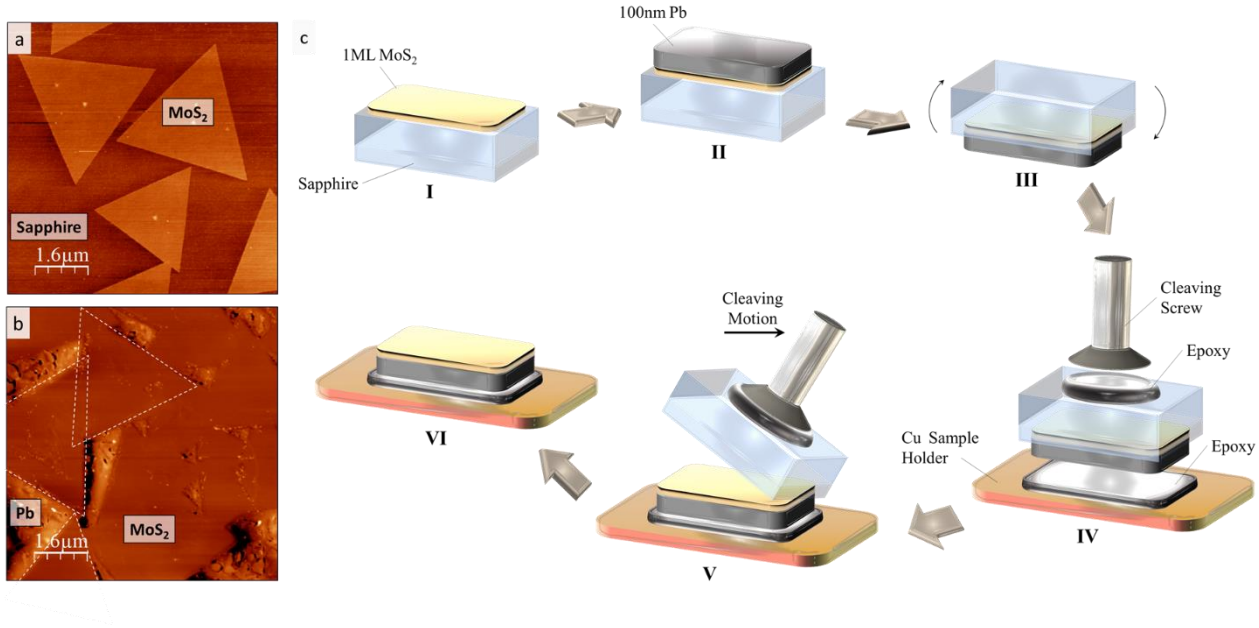

Figure S1| Fabrication steps for MoS_2/Pb sample. **a,** AFM topography of the as-grown MoS_2 film on the sapphire substrate. **b,** AFM topography of the MoS_2 film on the Pb substrate following the fabrication process in Fig. S1c. White dashed lines are a guide to the eye for the estimated position of the triangular MoS_2 islands. **c,** Sample fabrication steps.

II. Reference Sample Characterization

A 150 nm Pb film was produced on a sapphire substrate as a reference film using the same deposition parameters as those used for depositing the Pb film on MoS_2 films. This *ex-situ* fabricated film was then transferred to the UHV system that houses the STM. The surface oxide layer on the film was removed by using argon-ion back-sputtering in UHV at 1 keV for 10 minutes using 2 μA beam current and 2 mm x 2 mm beam size. The resulting surface was measured using scanning tunneling spectroscopy. The temperature dependence of the spectra acquired from this sample is shown in Fig. S2. The critical temperature is found to be 7.1K.

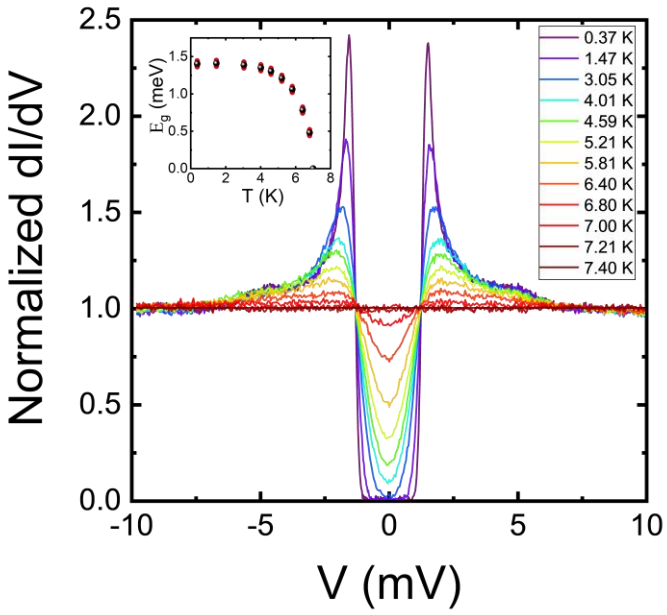

Figure S2| Reference Pb T_c characterization. Evolution of the low-energy tunneling spectrum as a function of sample temperature (V_{set} = 10 mV, I = 100 pA, V_{mod} = 0.2 mV). All spectra are normalized to the normal-state spectrum measured at 7.4K. The inset shows the evolution of the superconducting gap as a function of temperature obtained by fitting the spectra using the BCS-Dynes formula.

III. Raman Measurements

All Raman measurements performed on Pb/MoS_2 twin samples were carried out using a Renishaw InVia Raman microscope with 514 nm laser source, 10 s exposure time, 10 mW power and 50X objective lens. Experimental data are shown in Fig. S3 and we consider the Raman study of Nayak *et al*[1] (532 nm laser) for comparison. The Nayak *et al*[1] work examined the 1T' phase in which they observed the J2 and J3 peaks around 225 cm^{-1} and 325cm^{-1}, respectively. These are the two of the signature peaks of both the T and T' phase.[2,3] In contrast, our data show no evidence of either of these peaks and we are therefore able to conclude that our monolayer films are 2H-MoS_2.

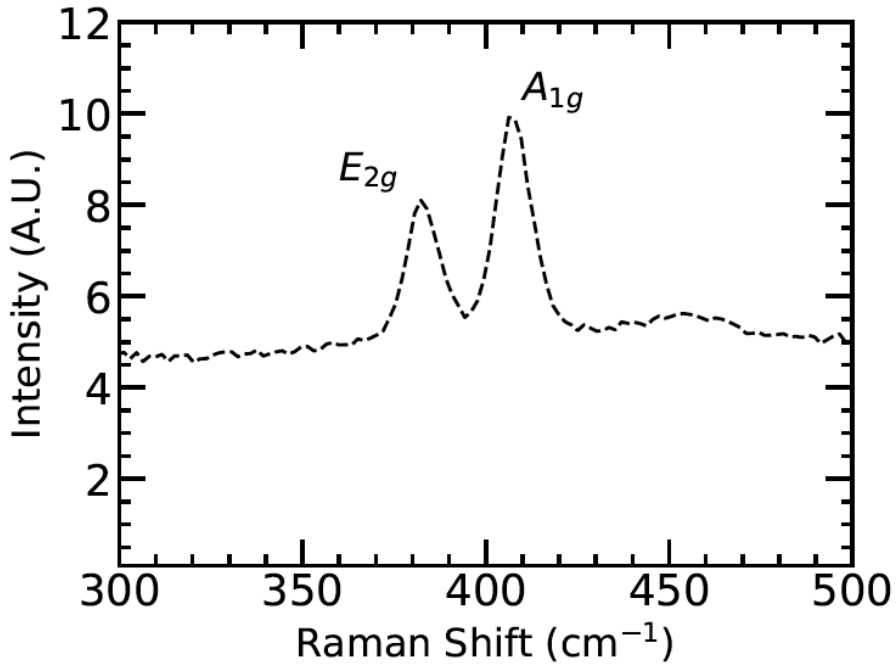

Figure S3| Raman characterization. Raman spectrum taken from MoS_2 monolayer on Pb showing characteristic E2g and A1G peaks. Comparison with the work of Nayak *et al*.[1] indicates that the monolayer is 2H-MoS_2.

IV. Modified Lawler-Fujita Strain Analysis

In order to assess the strain in the MoS_2 film, we use a modified, real-space, Lawler-Fujita algorithm[4,5] to identify the real-space atomic positions in STM topography maps such as those in Fig. S4a. After a careful piezo calibration on a known lattice, we compared the atomic positions with those of an ideal, unstrained lattice of MoS_2 (lattice parameter 3.2 Å). This comparison is shown in Fig. S4b. The displacement field, shown in Fig. S4c, is the difference between the two lattices in Fig. S4b that is broken down into its horizontal (X-direction) and vertical (Y-direction) components as a function of position. The strain is derived from the displacement field as the derivative with respect to x and y directions. The slope of the best fit line of the two components of the displacement field yields the average strain along these directions. For comparison, displacement fields corresponding to a tensile and compressive strain of 1% are plotted in Fig. S4c as black- and blue-dashed lines, respectively. Using this method, the X- and Y-strain on the MoS_2 film is estimated to be 0.53% and 0.60%, respectively.

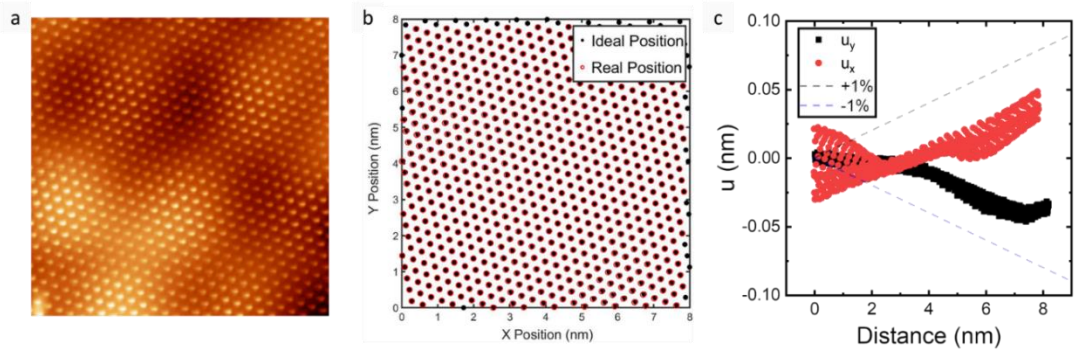

Figure S4| MoS_2 lattice parameter determination. **a,** Atomic resolution STM topography (8nm x 8nm) showing the top S atoms of the MoS_2 film (V = 10 mV, I = 100 pA). **b,** Real-space identification of atomic positions (red open circles) and comparison with the ideal atomic positions in unstrained MoS_2 (black circles). **c,** The vertical (u_y–black squares) and horizontal (u_x-red circles) components of the displacement field obtained from the comparison of real and ideal lattice in Fig. S4b. The black- and blue-dashed lines represent the displacement field corresponding to a tensile and compressive strain of 1%, respectively.

V. STM Topography Images

Figure S5 shows constant-current STM topography images of MoS_2 on Pb at different bias voltage. A moiré pattern with a period of 3.3 nm is clearly visible at all bias voltages between +1 V and -1 V. By aligning the topographic images it can be seen that the peak positions of the moiré pattern (bright regions) are independent of bias voltage. The apparent peak-to-peak corrugation of the moiré pattern is 5 pm at +1 V and 2 pm at -1V and 10 mV.

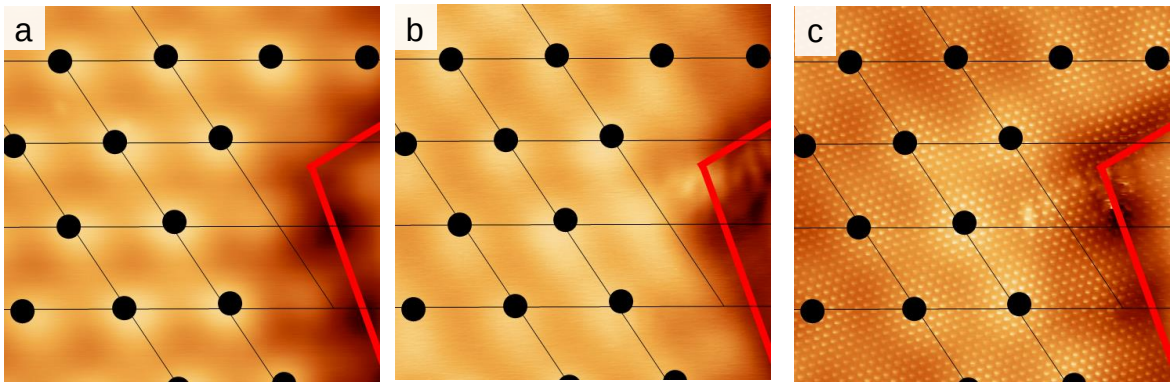

Figure S5| STM Topography images. a-c, STM topography acquired in the same location with bias voltages V= +1V, -1V and 10 mV, respectively. Black circles represent position of the peaks in the moiré pattern in (a). These black circles are copied to the topographies in (b) and (c) after aligning the red lines with the kink in the grain boundary region.

VI. Relationship Between the Present Model and McMillan-Arnold Formalism

It is instructive to compare our atomic-scale tight-binding model to coarse-grained models of McMillan[6] and Arnold[7] that have led to the concepts of Andreev reflection and Andreev bound states. We follow the terminology of De Gennes[8] for describing the superconducting state. The most important input parameter is the pair-potential Δ (order parameter), which may be dependent on real-space position or it may be a matrix in an atomic-orbital basis. The key outcome in characterizing the superconducting state is the condensation amplitude $F(E)$ (anomalous Green's function), which gives the probability amplitude of finding two electrons in the condensed state at a given position or, in an atomic-orbital basis, the pairing correlation between the various orbitals.

The corresponding quasiparticle spectrum obtained from the regular Green's function G(E) can be used to determine the energy gap, E_G, which is the lowest quasiparticle excitation energy. G(E) can also be used to analyze the coherence peaks in the spectrum to gain a deeper understanding of the superconducting state.

The coarse-grained approach is based on invoking the presence of a tunneling potential barrier between the superconducting (S) and normal metal (N) subsystems where the effective thickness d of the N side, the superconducting coherence length ξ, and the difference between the effective pairing potentials Δ_N and Δ_S determine the energies of the bound states within the N subsystem. In principle, the order parameters include an intrinsic part and a proximity induced part, $\Delta_N = \Delta_N^{ph} + \Delta_N^{ind}$ and $\Delta_S = \Delta_S^{ph} + \Delta_S^{ind}$, where superscripts 'ph' and 'ind' denote the intrinsic (phonon) and induced components. In Arnold approach, one can start from $\Delta_N^{ph} = 0$ and a non-zero Δ_S^{ph} and then self-consistently calculate the new intrinsic and induced order parameters. Ref. [7] shows how the order parameters emerge from Bogoliubov-deGennes (BdG) equations[9] and Nambu-Gorkov Green's function techniques[10], where the S and N sides are described as independent subsystems, and the interaction between the two sides is described by using a self-energy matrix, which can be converted to renormalization factors and effective order parameters.

The Hamiltonian of Eqs. T1 and T2 of the main text can be written in the form of BdG equations:

$$H_0 u + \Delta v = E u$$

$$\Delta^\dagger u - H_0^\dagger v = E v$$

where u and v are the electron and hole wavefunction vectors in a tight-binding basis, H_0 is the normal-state Hamiltonian matrix and Δ is the pair-potential matrix. In the present model, the pair potential is given as an input parameter, which is non-zero in the SC side only, and it should not

be equated with the parameters Δ_S and Δ_N. The Nambu-Gorkov Green's function may be solved from the BdG equations to obtain both its regular and anomalous components.

In order to see the connection with the Arnold approach, one can transform the present BdG equations into separate equations for the S and N sides, where the subsystem S (or N) is coupled through Dyson's equation to the subsystem N (or S) as a self-energy matrix (see Ref. [7]):

$$(H_0 + \Sigma_{11})u + (\Delta^{ph} + \Sigma_{12})v = Eu$$

$$(\Delta^{ph} + \Sigma_{12})^{\dagger}u - (H_0 + \Sigma_{11})^{\dagger}v = Ev$$

where $\sum_{11}^{N}(E) = H_{NS}G_{SS}^{0}(E)H_{SN}$ and $\sum_{12}^{N}(E) = -H_{NS}F_{SS}^{0}(E)H_{SN}^{\dagger}$ for the N subsystem, and similar equations arise for the S subsystem with the regular and anomalous Green's functions calculated for the S and N subsystems independently. The resulting pair potentials for the two subsystems then are: $\Delta_N = \Delta_N^{ph} + \Sigma_{12}^{N}$ and $\Delta_S = \Delta_S^{ph} + \Sigma_{12}^{S}$.

Note that the condensation amplitude in the tight-binding basis, $F_{\alpha\beta}(E)$, is non-local and the coherence length ξ is related to the decay rate of its off-diagonal matrix elements in real space. However, the corresponding pair potential may change quite abruptly across the interface: the matrix elements of the self-energy are non-zero only for orbitals at the interface which are defined in terms of the non-zero interaction matrix elements of H_{NS}. Hence the tight-binding model without any self-consistent phonon-electron coupling will yield for the normal side, $\Delta_N = \Delta_N^{ph} = 0$ at the Molybdenum and surface Sulphur layers, and $\Delta_N = -H_{NS}F_{SS}^{0}(E)H_{SN}^{\dagger}$ for the interface Sulphur layer. For the entire subsystem S, $\Delta_S = \Delta_S^{ph}$, since $F_{NN}^{0}(E) = 0$. Translating these considerations into the language of McMillan/Arnold this implies that the emergence of Andreev bound states is

possible only if $\Delta_N < \Delta_S$, a condition that is obviously fulfilled in our tight-binding approach to the present MoS_2 on Pb heterostructure.

Although we cannot quantitatively predict the shift between the moiré pattern in the topographic map and the scaled conductance map seen in Fig. 3(a), we can identify the factors behind the different modulations in the two maps using our atomic-scale analysis. The self-energy description of the substrate described above relates the local atomic configuration of the interface to the transmission properties of the interface and hence to the modulation in the two aforementioned maps. The topographic STM image is obtained in the *constant current mode* and it is thus a mapping of the regular part of the Green's function $G_{NN}(E)$ of the overlayer[10–12], and it is dominated by the regular self-energy $\sum_{11}^{N}(E) = H_{NS}G_{SS}^{0}(E)H_{SN}$. The local gap properties of induced superconductivity, however, are strongly dependent on the effective pairing-potential of the overlayer $\Delta_N = \Delta_N^{ph} - H_{NS}F_{SS}^{0}(E)H_{SN}^{\dagger}$. The role of local geometry of the interface is included in the orbital overlaps H_{NS} between the p-orbitals of S and Pb atoms across the interface. While this is the common factor relating moiré patterns to the local geometry, there is no reason for G_{SS}^{0} and F_{SS}^{0} to follow the same symmetry and orbital contributions, and hence the modulation in the regular LDOS and the superconducting pairing of the overlayer will, in general, follow separate patterns.

In order to gain insight into the nature of the regular and anomalous components of the Green's functions, we compare in Fig. S6 their onsite and next-nearest-neighbor-atom matrix elements between the p_x and p_z orbitals. The relative spectral weights of the imaginary parts of the p_x-p_x vs. p_z-p_z matrix elements are seen to scale rather similarly for both the regular and the anomalous case. In contrast, the spectral weights of the real parts of the regular and anomalous matrix elements may scale quite differently since the real part of the regular Green's function of

the substrate is offset from zero, while the real part of the anomalous matrix element approaches zero outside the gap. Figs. S6(c) and S6(e) show the amplitude-squared of the p_x-p_x matrix element scaled by the onsite p_z-p_z matrix element. The most striking feature is the symmetry of the scaled anomalous matrix element, while the corresponding regular matrix element as a function of energy has much more structure. We speculate that if the phonon-electron coupling were included in accounting for superconductivity, the heterogeneity of the interface could create locally modulated phonon modes, which would then further modulate the intrinsic pairing potential Δ_N^{ph}. One approach to quantify the formation of different moiré patterns would be to spatially average the tight-binding self-energy terms and apply the coarse-grained transmission terms in the continuum models of Andreev reflection.

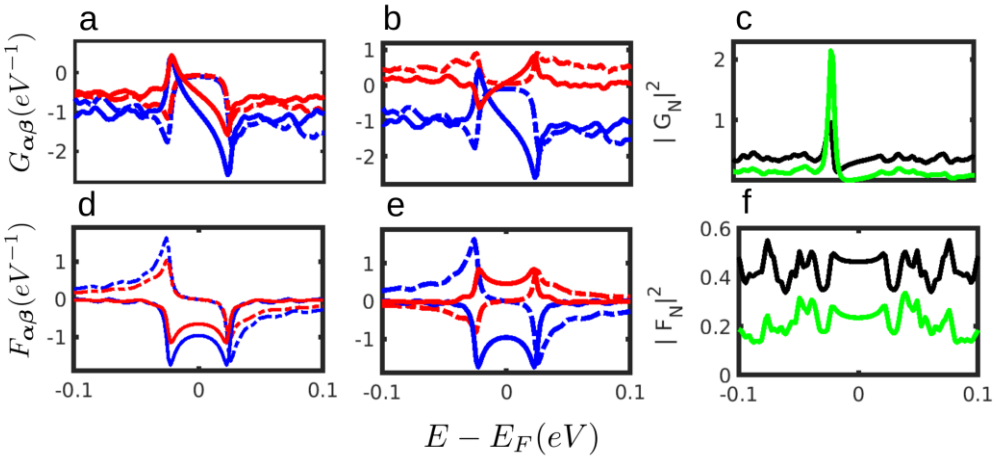

Figure S6| Regular and anomalous matrix elements of Nambu-Gorkov Green's function. Imaginary (dashed) and real (solid lines) parts of the matrix elements of the regular (**a-b**) and anomalous (**d-e**) Green's function. As a reference, the blue curves in each subfigure show the onsite p_z-p_z matrix element of the Green's function. In **a** and **d** shown in red is the onsite p_x-p_x matrix element, **b** and **e** show the next-nearest-neighbor p_x-p_x element; **c** and **f** show the square of the normalized absolute value of the regular ($|G_N|^2$) and anomalous ($|F_N|^2$) matrix-element of Green's function, respectively. Black curve shows the onsite p_x-p_x element normalized by p_z-p_z element, while the green curve shows the next-nearest-neighbor p_x-p_x element normalized by the onsite p_z-p_z.

VII. Arnold theory of the Proximity Effect

The Arnold[7] model is an exact solution of the single-particle Green's function for a Superconductor/Normal metal (S/N) bilayer. The principal assumptions are that the S and N layers are electrically well coupled and that the interface transmission is specular. This reduces the solution to a 1-d problem for electrons propagating normal to the interface with appropriate boundary conditions. For the case where the N layer thickness, d, is much smaller than the superconducting coherence lengths in the S and N layers (ξ_S, ξ_N), the spatial dependence of the gap parameters, Δ_S and Δ_N can be ignored to leading order. The generic step picture similar to that discussed in Ref. 7 is shown in Fig. S7. The induced superconducting gap in the N layer, Δ_N, can, in principle, be determined self-consistently using bulk properties of the N layer.[13]

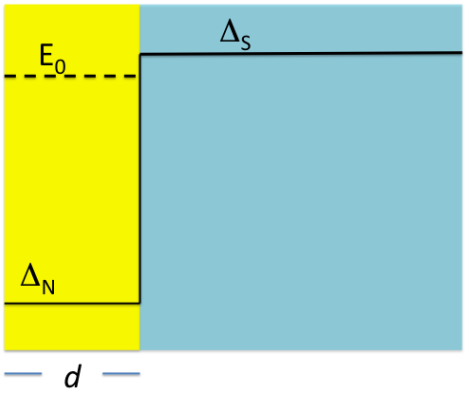

Figure S7| Step model for spatially constant pair potentials in the thin-N limit. Bound state at E_0 is indicated and, in general, it is quite close to the superconductor gap parameter, Δ_S. In the original Arnold paper the N-layer thickness is denoted by d_N but in the present paper we use *d* for convenience.

Quasiparticle excitations above Δ_N, which would be a continuum in a bulk system, are now reduced to a discrete set of bound states due to the confinement in the potential well given by Δ_S - Δ_N. The problem is similar to that of an ordinary (finite) potential well in quantum mechanics, except that here the reflection at the N/S interface involves Andreev scattering in which an electron-like quasiparticle reflects as a hole-like quasiparticle and vice-versa. These discrete states are the Andreev bound states. For the thin N-layer case there is only one bound state at energy E_0 just below Δ_S.

There are two parameters in the original Arnold theory[7] that determine the number and energies of all bound states. The first is $R = 2d/\hbar v_F$, where v_F is the Fermi velocity in the N-layer renormalized by the electron-phonon interaction. Here, we will treat R as an adjustable parameter. The other parameter is the well-depth, Δ_S - Δ_N. Consistent with our DFT-based analysis that shows a decrease in the pair potential across the MoS_2 layer, we will assume that Δ_N is small and fix its value to 0.001 meV. This allows the presence of a potential well and the existence of the related bound state at the interface. We emphasize, however, that our main conclusions are not sensitive to our choice of the absolute value of Δ_N, because we can adjust the R values to obtain the same fits for the experimental intensities of high and low peaks. The quasiparticle density of states (DOS) at the surface of the N-layer relevant for STS spectra of Pb/MoS_2 is shown in Fig. S8 using the Pb gap parameter (1.38 meV) with R values ranging from 0.04 to 0.2 meV^{-1}. For increasing R value, the Andreev bound state is pulled down further below Δ_S and shows up as a sharp peak in the DOS. We account for scattering of quasiparticles in the N layer by introducing a mean free path, l, and choose a value of d/l = 0.03, which is sufficient to broaden the bound state singularity into a Lorentzian-type peak. There is also a sharp decrease in the DOS between E_0 and Δ_S. Note that the loss of states in the continuum above Δ_S shows up in the bound state peak to

conserve states. As R decreases, the Arnold DOS merges with the BCS DOS. To fit the experimental STS data, we obtained the normalized dynamical conductance (dI/dV) by using the proximity DOS convoluted with the Fermi function.

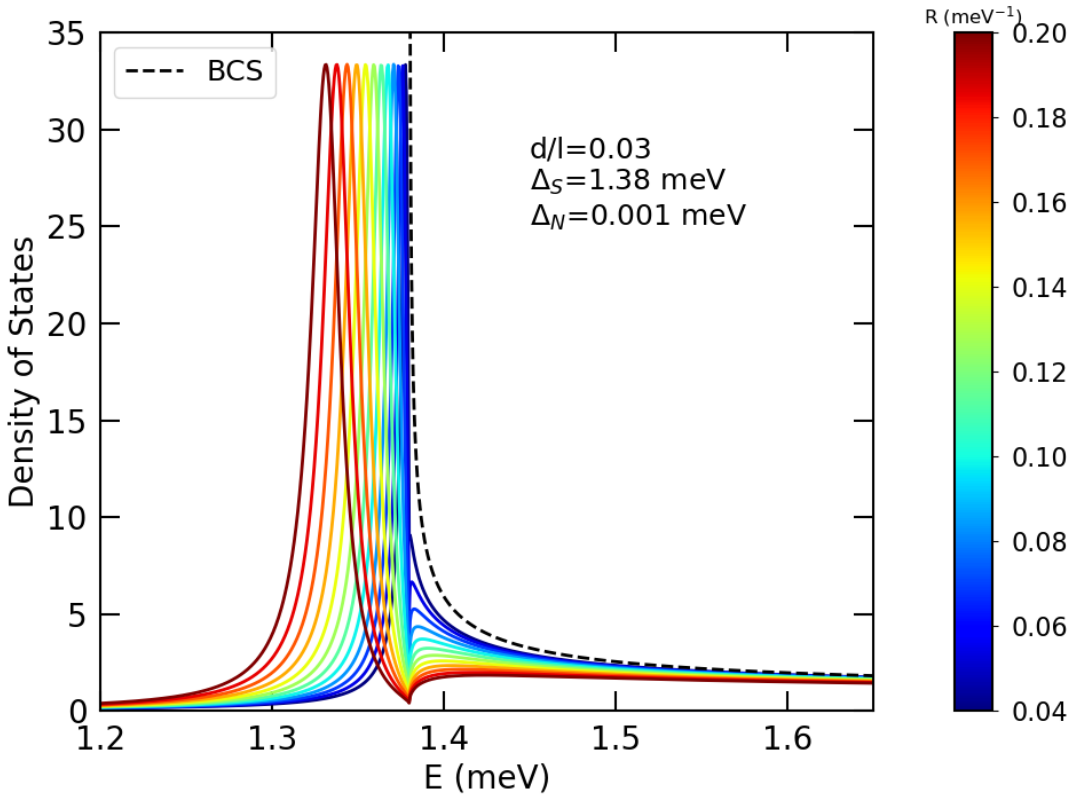

Figure S8| Arnold proximity DOS. Arnold proximity DOS compared to BCS DOS (dashed blue line) for various R values showing the distinct Andreev bound state below Δ_S, which is seen more clearly for larger R values.

Fig. S9 shows the normalized conductance at T = 1.5 K for three different R values. It can be seen that for relatively large $R = 0.45\ meV^{-1}$ the bound state produces a much higher normalized conductance peak compared to BCS, but since states are conserved, the conductance is below BCS

above Δ_S. In the other extreme of relatively small $R = 0.0045\ meV^{-1}$ the Arnold fit (red curve) is *nearly identical* to that obtained with a BCS DOS (blue dashed line). For $R = 0.09\ meV^{-1}$ the bound state produces a peak that is somewhat higher than BCS and at a voltage close to the Pb gap.

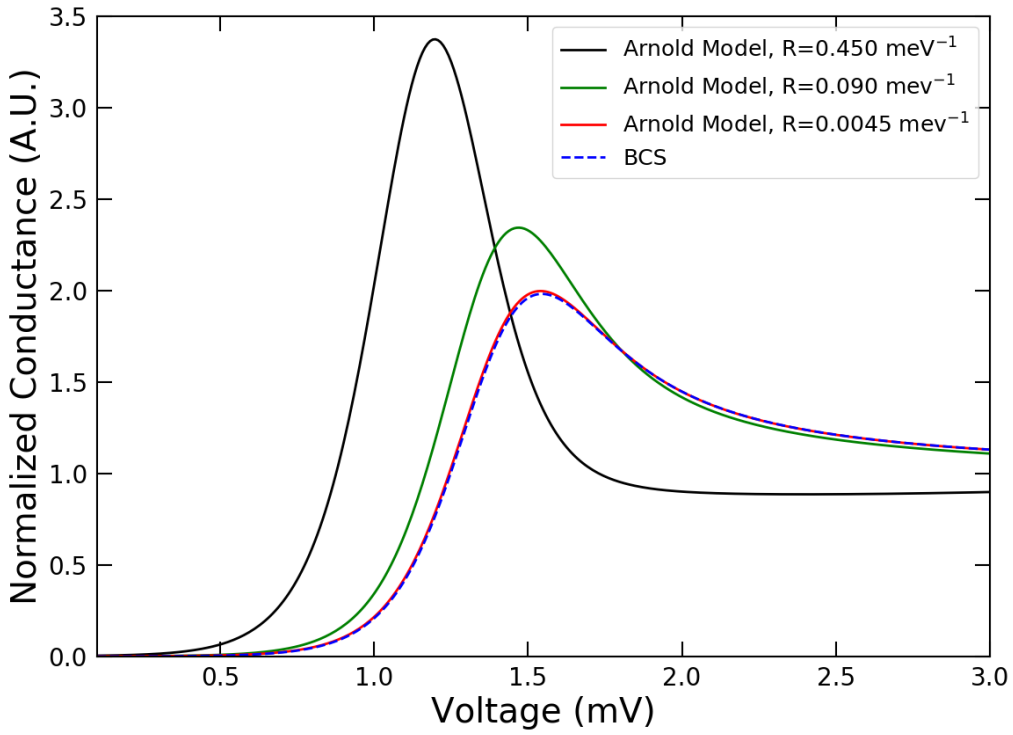

Figure S9| Calculated normalized conductance for the Arnold DOS. Normalized conductance calculated with three different values of R is compared with the BCS DOS.

The Arnold model thus captures the variation in the normalized STS conductance peak observed in our experiments as being due to a changing value of R across the moiré pattern. Further discussion, however, is needed to understand what causes changes in the R values. We address

this by turning to an extension of the original Arnold theory [14] that treats a *normal, electrostatic* potential step at the N/S interface and takes into account the differences in electronic structure and Fermi velocity in the S and N layers. Such a potential step leads to an additional, ordinary reflection coefficient *r* at the interface. The bound state then depends on $R_{eff} = \left(\frac{1+r}{1-r}\right) R$. Since the atomic moiré pattern indicates a periodic variation in the atomic orbital overlap, it is reasonable to expect a periodic variation in the reflection coefficient as well that not need be commensurate with the atomic moiré. In our analysis, since the low-conductance peak is close to the BCS result, we choose r = 0. For the high peak, Fig. S8 shows that we need a larger R_{eff} and this is achieved with r = 0.5. Our analysis clearly that an Andreev bound state is being seen with STS and that the Arnold theory provides a reasonable explanation of the observed spectra.

REFERENCES

(1) Nayak, A. P.; Pandey, T.; Voiry, D.; Liu, J.; Moran, S. T.; Sharma, A.; Tan, C.; Chen, C.-H.; Li, L.-J.; Chhowalla, M.; Lin, J.-F. Pressure-Dependent Optical and Vibrational Properties of Monolayer Molybdenum Disulfide. *Nano Letters* **2015**, *15*, 346–353.

(2) Yu, Y.; Nam, G.-H.; He, Q.; Wu, X.-J.; Zhang, K.; Yang, Z.; Chen, J.; Ma, Q.; Zhao, M.; Liu, Z.; Ran, F.-R.; Wang, X.; Li, H.; Huang, X.; Li, B.; Xiong, Q.; Zhang, Q.; Liu, Z.; Gu, L.; Du, Y.; Huang, W.; Zhang, H. High Phase-Purity 1T′-MoS_2- and 1T′-$MoSe_2$-Layered Crystals. *Nature Chemistry* **2018**, *10*, 638–643.

(3) Gupta, U.; Naidu, B. S.; Maitra, U.; Singh, A.; Shirodkar, S. N.; Waghmare, U. V.; Rao, C. N. R. Characterization of Few-Layer 1T-$MoSe_2$ and Its Superior Performance in the Visible-Light Induced Hydrogen Evolution Reaction. *APL Materials* **2014**, *2*, 092802.

(4) Lawler, M. J.; Fujita, K.; Lee, J.; Schmidt, A. R.; Kohsaka, Y.; Kim, C. K.; Eisaki, H.; Uchida, S.; Davis, J. C.; Sethna, J. P.; Kim, E.-A. Intra-Unit-Cell Electronic Nematicity of the High-Tc Copper-Oxide Pseudogap States. *Nature* **2010**, *466* (7304), 347–351.

(5) Trainer, D. J.; Zhang, Y.; Bobba, F.; Xi, X.; Hla, S.-W.; Iavarone, M. The Effects of Atomic-Scale Strain Relaxation on the Electronic Properties of Monolayer MoS_2. *ACS Nano* **2019**, *13*, 8284–8291.

(6) McMillan, W. L. Tunneling Model of the Superconducting Proximity Effect. *Physical Review* **1968**, *175*, 537–542.

(7) Arnold, G. B. Theory of Thin Proximity-Effect Sandwiches. *Physical Review B* **1978**, *18* , 1076–1100.

(8) De Gennes, P. G. Boundary Effects in Superconductors. *Reviews of Modern Physics* **1964**, *36*, 225–237.

(9) Abrikosov, A. A.; Gorkov, L. P.; Dzyaloshinkii, I. *Methods of Quantum Field Theory in Statistical Physics*; New York, NY: Dover, 1975.

(10) Tersoff, J.; Hamann, D. R. Theory of the Scanning Tunneling Microscope. *Physical Review B* **1985**, *31*, 805–813.

(11) Todorov, T. N.; Briggs, G. A. D.; Sutton, A. P. Elastic Quantum Transport through Small Structures. *Journal of Physics: Condensed Matter* **1993**, *5*, 2389–2406.

(12) Pendry, J. B.; Pretre, A. B.; Krutzen, B. C. H. Theory of the Scanning Tunnelling Microscope. *Journal of Physics: Condensed Matter* **1991**, *3*, 4313–4321.

(13) Arnold, G. B.; Zasadzinski, J.; Osmun, J. W.; Wolf, E. L. Proximity Electron Tunneling Spectroscopy. II. Effects of the Induced N-Metal Pair Potential on Calculated S-Metal Properties. *Journal of Low Temperature Physics* **1980**, *40*, 225–246.

(14) Wolf, E. L.; Arnold, G. B. Proximity Electron Tunneling Spectroscopy. *Physics Reports* **1982**, *91*, 31–102.